Mechanical Behaviour of Compacted Dutch Clays

Compositional Effects and Suitability for Dike Reinforcement

Leen S. Ar. Al-Hijjawi

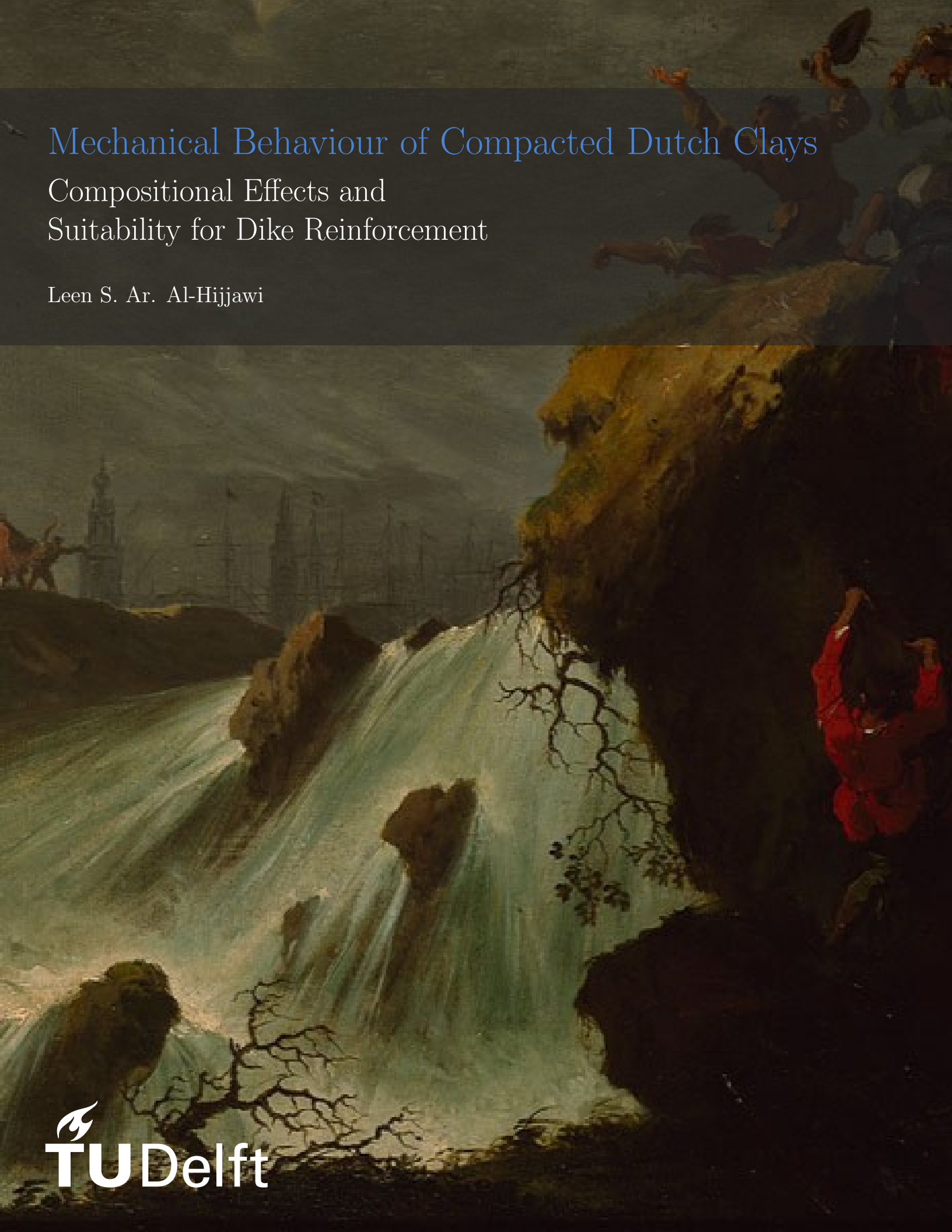

TU Delft

Mechanical Behaviour of Compacted Dutch Clays

Compositional Effects and Suitability for Dike Reinforcement

by

Leen S. Ar. Al-Hijjawi

In partial fulfilment of the requirements for the degree

Master of Science

at Delft University of Technology

Faculty Of Civil Engineering and Geosciences

Student number:	5849969	
Project duration:	January, 2024 – August, 2024	
Thesis committee:	Dr. L. (Luca) Flessati,	TU Delft, Chair
	Dr. S. (Stefano) Muraro,	TU Delft, Main supervisor
	Prof. dr. C. (Cristina) Jommi,	TU Delft
	Dr. C. (Claire) Chassagne,	TU Delft

This thesis is confidential and cannot be made public until December 31, 2025.

Cover: Willem Schellinks' painting, "De doorbraak van de Sint Anthonisdijk bij Houtewael" Credit: public domain.

TU Delft

Abstract

The Netherlands faces an urgent need to reinforce its flood defences against rising sea levels. This study investigates the potential of using locally sourced Dutch clays as a sustainable alternative to imported materials for dike reinforcement. A comprehensive experimental campaign was conducted on three types of laboratory-compacted Dutch clays, with clay content varying from 42% to 23% and differing levels of erodibility. Soil characterisation, microstructural analysis (ESEM), and mechanical testing through oedometer and triaxial tests assessed the impact of composition on engineering properties. Results showed that compression behaviour is primarily influenced by the clay content, while shear response, exhibiting both contractive and dilative tendencies, remained consistent across the different compositions. Triaxial tests revealed that samples acted as representative volume elements (RVEs) only up to a certain strain level, beyond which localised deformations occurred due to end-restraint. Additionally, mixing local soils with erosion-resistant materials proved effective in improving the erodibility of unsuitable soils, thereby reducing the quantity of imported material needed. Finally, a new advanced model, JMC-clay bounding surface, was calibrated and validated across the range of soil compositions. The model accurately captured pre-failure and failure behaviour, demonstrating its applicability for predicting geotechnical structure performance and stability.

Acknowledgements

With sincere gratitude, I would like to thank the individuals who have shaped and supported my journey. First and foremost, I extend my deepest thanks to my main supervisor, Dr. Stefano, for his time, mentorship, and unwavering support. A special thanks to Prof. Jommi for her guidance and insights, Dr. Luca and Dr. Claire, for their valuable feedback. Special recognition goes to Ching-Yu for his expertise in navigating the complexities of the model, and Luis for his invaluable assistance in the lab. I also extend my appreciation to Sian for facilitating the CT scans, Arjan for his support with the electron scanning microscope, and the Rivierwerken project team (M. Barciela, C. McLoed) for supplying the material.

And finally, to Samir, Layla, Amr, and Dana, for their unconditional love and encouragement, and to the remarkable friends I've made in Delft, and all the wholesome encounters along the way - thank you all for being a part of this journey.

Table of Contents

List of Figures

List of Tables

Chapter 1

Introduction

1.1 Background

The Netherlands has a long history of utilizing dikes for flood protection and land reclamation, with the earliest dikes dating back to the beginning of the first millennium. These initial constructions were modest in scale, often consisting of stacked clay or sandy salt marsh sods sourced directly from the surrounding environment (Schaafsma-Tilstra, 2014). Constructed from locally available materials such as clay, sand, and peat, the varying compositions of these early dikes influenced their strength and durability. As the need for flood protection grew, so did the complexity of dyke construction. Later medieval dikes continued to utilise clay or sand cores but incorporated a clay overlay for added strength.

In the face of rising sea levels and the escalating challenges of the global climate crisis, maintaining the integrity of dike systems in the Netherlands has become increasingly crucial. The low-lying geography of the Netherlands makes it particularly vulnerable to flooding (Fig. 1.1), necessitating robust and resilient dike systems. Consequently, there is a heightened focus on strengthening these critical structures. The Dutch Flood Protection Programme (HWBP, 2023) exemplifies the Netherlands' proactive approach to future-proofing its flood defences. This comprehensive initiative aims to enhance the country's flood defences by 2050 by reinforcing approximately 2000 kilometres of primary barriers (i.e., dikes, dams, and dunes). The dike reinforcement involves several strategies, including elevation and widening (den Heijer & Kok, 2024).

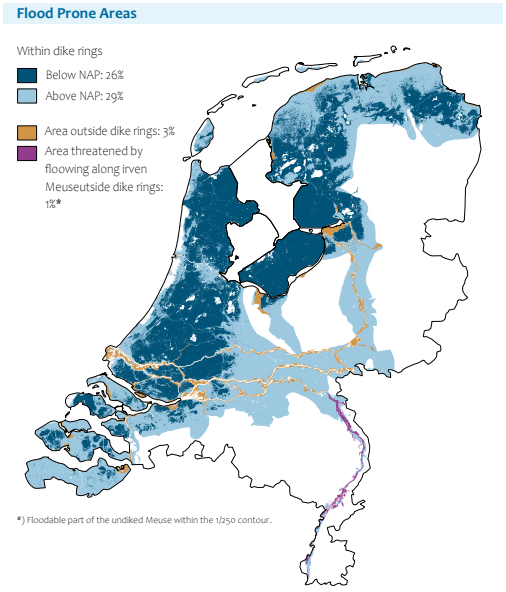

Figure 1.1: Flood prone areas - (Netherlands Environment Assessment Agency, 2019)

Today, the selection of materials for dike strengthening is guided by criteria designed to ensure optimal safety and durability. These criteria categorise soils into three groups based on their erosion resistance, determined through simple soil characterisation tests that consider soil composition and field placement conditions. Traditionally, the Netherlands has relied heavily on importing high-quality soil when local soil

does not meet these criteria. Nowadays, this practice presents several challenges, including the scarcity of naturally erosion-resistant clay within the region and the financial and environmental costs associated with transporting suitable materials. Consequently, there is a need to reassess current practices.

1.2 Problem Statement

Meeting the safety standards by 2050 for Dutch dikes is a massive undertaking that demands substantial quantities of raw materials. However, using local soil is challenging due to regulatory constraints. Despite recent initiatives promoting sustainable practices, the Netherlands still predominantly relies on a standard-driven design approach, unlike other European countries that have adopted a ground-driven design approach (Wiggers & Peters, 2021). This alternative approach allows for greater flexibility by tailoring the dike design to the specific properties of the available local soil, rather than trying to modify the soil to fit a predetermined design (Fig. 1.2).

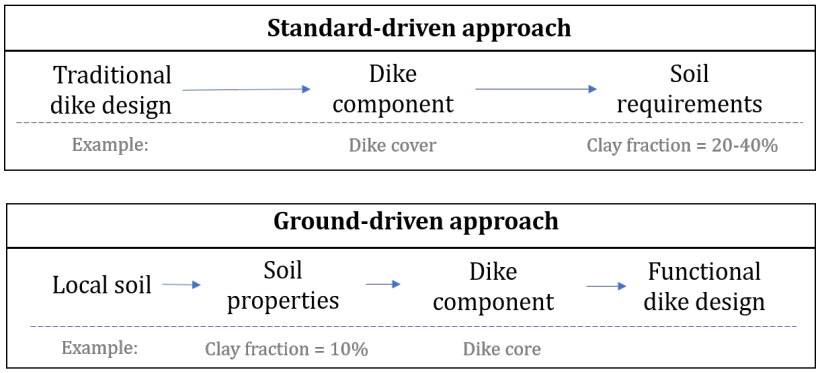

Figure 1.2: Standard- and soil-driven design processes

The adoption of a ground-driven design approach begins with a thorough understanding of the characteristics of the soils used, as this directly impacts the durability of these critical structures. To ensure compliance with ultimate limit states (ULS) and serviceability limit states (SLS) in geotechnical design and assessment, it is essential to obtain reliable data that accurately describes both the pre-failure and failure behaviour of soils. However, the inherent variability in soil composition complicates the understanding and prediction of their mechanical responses. Therefore, it is essential to identify how varying soil compositions affect the mechanical behaviour, particularly under compression and shear. The shear strength and deformation characteristics of soils directly impact their ability to withstand environmental and anthropogenic stresses without experiencing significant deformation or failure. This factor is essential in dike construction and maintenance, where structural integrity and stability are fundamental.

One potential solution to overcome the limitations of local soils with low erosion resistance is to mix them with imported erosion-resistant clay to enhance their mechanical properties and meet the required standards for dike construction (Fig. 1.3). This approach has been adopted in the ceramics industry to improve the workability of lower plasticity clay (Barnes, 2018), but has not been extensively studied in dike reinforcement applications.

(a) (b)

Figure 1.3: Clay mixing (a) Dike reinforcement works at dike ring 59 (Bergen-Aijen) Image courtesy of C. McLeod (b) Clay mixing at Delgromi depot for use in brick production ("Delgromij", n.d.)

Through blending local and imported clay, it is possible to achieve a balance between utilising available resources and meeting the construction standards. This approach can serve as a step forward to address the scarcity of high-quality construction materials and contribute to the sustainability of flood protection measures by reducing emissions associated with transportation in addition to conserving natural resources.

Chapter 2

Literature Review

This chapter synthesises existing research on the engineering properties of clays and silty clays, focusing on characteristics relevant to dike construction. The review encompasses relevant Dutch assessment standards for dike material and the impact of compositional variations on soil behaviour. Additionally, the chapter explores the microstructural aspects of compacted clays, providing a foundation for understanding their performance in dike applications.

2.1 Engineering Properties of Clay Used in Dikes

As discussed in Chapter 1, the selection of materials for dike strengthening is mainly governed by criteria based on erosion resistance. However, characterising the erosion resistance of fine-grained soils is challenging due to the numerous parameters that control their erosion behaviour. Key properties affecting soil erodibility include (Mostafa et al., 2008):

- Physical and mechanical properties of the soil cover such as clay content, soil structure, compaction, and density.
- Chemical and electrochemical properties such as cation exchange capacity (CEC), salinity, pH levels, and clay mineralogy.
- Biological properties encompassing the nature and content of organic matter and its interactions with the clay-water system.
- Chemical and physical properties of eroding water such as salinity, pH, flow characteristics, and temperature.

While many factors influence the erosion behaviour of soil, the following sections will focus on key geotechnical parameters typically obtained in practice including particle size distribution, organic content, water content, and density.

Particle Size Distribution

Gravel, sand, silt, and clay fractions each play distinct roles in contributing to soil erosion resistance. The erodibility of gravels and sands depends on the balance between particle weight and the applied hydrodynamic force, as well as their mineral composition. This is particularly important for granular soils composed of carbonate minerals which can dissolve in the presence of carbon dioxide in water (Briaud et al., 2019).

In clayey soils, individual clay particles can form micro-aggregates (ranging from single to dozens of micrometres) and macro-aggregates (ranging from dozens to thousands of micrometres). The erosion behaviour of these soils is influenced by the presence of these aggregates in the soil matrix, the ability of the particles to coagulate, their size and shape, and the clay resistance to disaggregation when submerged in water. Additionally, the presence of clay particles in sand enhances bonding among the sand particles, significantly increasing the erosion resistance (Briaud et al., 2019).

The influence of silt on soil erodibility is marked by contradictory findings in the literature. For instance, Verhaegen (1984) reported that a higher silt content contributes to increased erosion resistance. In contrast, Briaud et al. (2019) noted that the silt fraction of soil is generally considered the least erosion-resistant.

Compaction Density & Moulding Water Content

Increased compaction moisture content and higher compaction density both lead to greater erosion resistance by reducing soil swelling and enhancing bonding forces between soil particles (Lyle and Smerdon, 1965; Paaswell, 1973; Hanson, 1992; Mostafa et al., 2008). However, the benefits of further compaction diminish beyond the optimum density, known as the maximum dry density, which is determined using the Proctor test. These findings emphasise the importance of optimising compaction and moisture content during construction.

Furthermore, if the clay used has a higher water content than the underlying unsaturated layer, then the suction exerted by the latter will cause the excess water in the upper clay to be drawn downward. As this water is removed, the clay will desiccate and contract, potentially leading to the formation of cracks that can significantly impact its functionality. Therefore, the workable water content of clay should lie above the optimum water content from the Proctor test and below the maximum allowable water content to prevent excessive drying and cracking (Delft, 1996).

Organic Content

Organic content, including microorganisms and organic matter, impacts soil erosion. Organic colloids can clog pores and reduce permeability, enhancing apparent cohesion and erosion resistance, particularly in coarse-grained soils (Guerra, 1994). However, high organic content can lead to significant shrinkage due to degradation, causing additional volume contraction (Delft, 1996).

Dutch Assessment Standards

The current standard in the Netherlands is based on extensive research conducted in the 1980s by Grondmechanica Delft, documented in the works by Kruse (1986) and Kruse (1987). However, the requirements for materials used in dikes have been updated over time (Fugro, 2021). Table 2.1 and Figure 2.1 present a summary of the current requirements, as outlined in *Handboek Dijkenbouw* (2018).

The primary criteria for classifying clay into different erosion resistance categories include the liquid limit (w_L), plasticity index (I_p), and sand content. The integration of the liquid limit and plastic limit in evaluating erosion resistance has been proposed and implemented by several studies (Gibbs, 1962; Kruse, 1988; Briaud et al., 2019; Fell et al., 2013).

Table 2.1: Overview of requirements for clay used in dikes in the Netherlands

Type	I	II	III
Property	Erosion-resistant clay	Moderately erosion-resistant clay	Low erosion-resistant clay
Liquid Limit (w_L)	$> 45\%$	$< 45\%$	$< 0.73(w_1 - 20)$
Plasticity Index (I_p)	$> 0.73(w_1 - 20)$	> 18	< 18
Sand Content		$< 40\%$	
Clay Content	20-40%	>8%	
Organic Material Content	3% - 5%	<5%	
Salt Content (NaCl g/l)		< 4	
Chalk Content (HCl loss)		$< 25\%$	
Colour & Smell	No extreme colour or strong smell		
Water Content	$I_c \geq 0.75$ (Top layer), $I_c \geq 0.60$ (Core)		
Compaction density	$\geq 97\%$ of Maximum dry density (Proctor Test)		

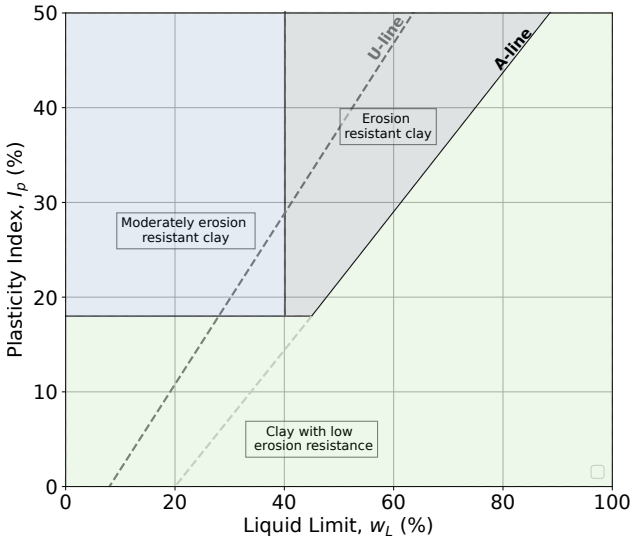

Figure 2.1: Plasticity chart for classifying erosion resistance

2.2 Compositional Effects

Natural soil deposits often contain particles of different sizes and base minerals, resulting in a wide range of compositions. These variations generally prevent the classification of natural soils into a single type (e.g., clay, silt, or sand), leading to combinations of these soil types. The formation process causes the particle size distributions to vary, and consequently, their mechanical behaviour can also differ.

Numerous studies have investigated the behavioural variations associated with different soil compositions, often by mixing standard clays or silts with clean sands in varying proportions. The results suggest that the mechanical behaviour of soils with mixed compositions reflects the combined characteristics of both constituents. Observations from these simpler systems help clarify how different particle sizes and types influence overall soil properties. The following sections summarise key findings from various studies on sand-clay and silt-clay mixtures, providing foundational insights for the study of more complex sand-silt-clay systems, which is the focus of this work.

2.2.1 Sand-Clay Mixtures

Research on sand-clay mixtures, such as the work by Muir Wood and Kumar (1999), has demonstrated the influence of composition on soil behaviour. In their study, triaxial tests on mixtures of kaolin clay and coarse uniform sand revealed that sand content does not significantly affect stress-strain and pore pressure responses until it exceeds 70% by mass. However, volumetric strains in drained triaxial compression tests were found to be sensitive to clay content variations within the range of 30% to 100%. The authors hypothesised that the mechanical response of these mixtures is primarily controlled by the clay matrix, especially at lower sand contents. To support this hypothesis, the volumetric strain specifically within the clay matrix was computed to find that the response remained largely independent of sand content until it reached 70% (Fig. 2.2). The authors added by saying, that after all, the sand particles are not predominantly in contact at the volume fractions of these tests and they merely form hard material which is not able to contribute to the deformational mechanism.

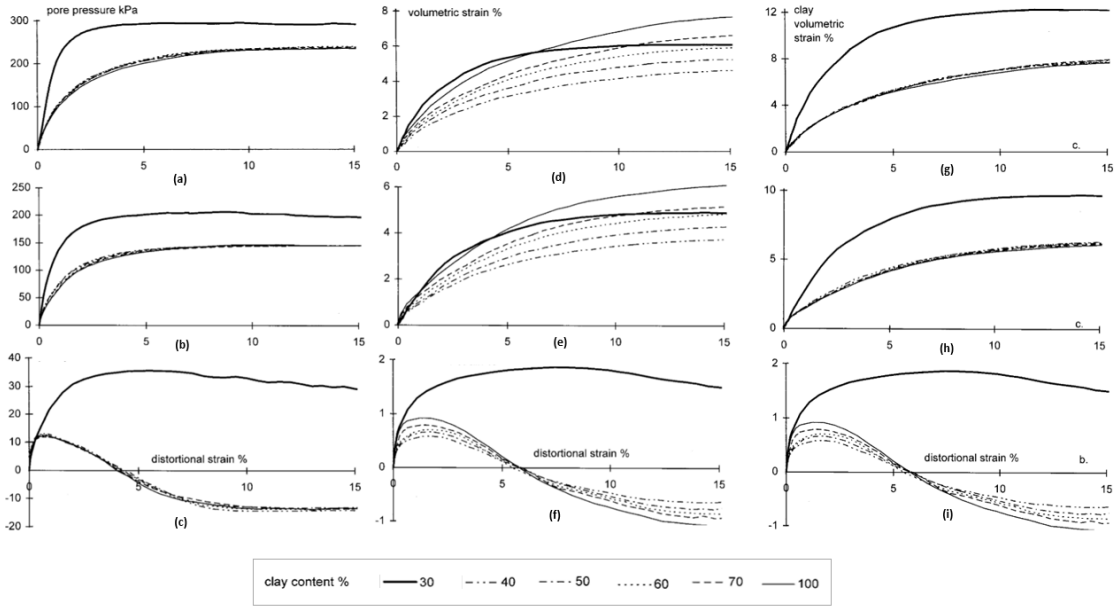

Figure 2.2: Pore pressure from undrained triaxial compression tests (a-c), volumetric strain (d-f), and clay volumetric strain (g-h) from drained triaxial compression tests on clay-sand mixtures at varying overconsolidation ratios (OCR = 1, 1.33, and 8 - top to bottom) - adapted from Muir Wood and Kumar (1999)

Monkul and Ozden (2007) studied kaolinite-sand mixtures and proposed a transitional fines content between 19% and 34%, where the behaviour of the soil matrix becomes dominated by the fines fraction. This transition significantly increases compressibility. They observed that coarser and finer grain matrices could rearrange into various modes depending on initial conditions and applied stress (Fig. 2.3)). At the transitional fines content, granular behaviour is established under direct grain contact.

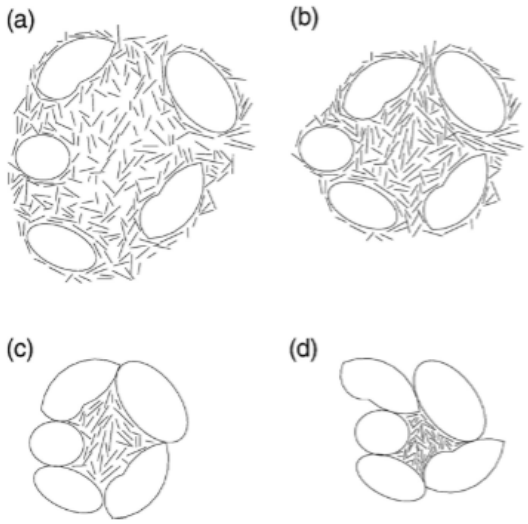

Figure 2.3: Different arrangements of matrices under 1-D compression - Monkul and Ozden (2007)

2.2.2 Silt-Clay Mixtures

Silt exhibits unique geotechnical properties that are intermediate between those of clays and sands. As silt content increases in silt-clay soils, they become less compressible compared to pure clays, under both one-dimensional and isotropic consolidation. (Yin, 1999; Cola and Simonini, 2002; Nocilla et al., 2006; Anantanasakul et al., 2012).

At high clay contents, silt-clay soils consist mainly of clusters of clay particles with some silt grains present. These silt particles do not interact with each other, making the soil matrix more compressible. Conversely, when the soil consists mainly of silt, the effective stresses are predominantly transferred among the larger and angular silt particles. The overall deformations of the soil matrix are influenced by the movements of these interconnected silt particles, resulting in a stiffer matrix (Anantanasakul & Roth, 2018).

Nocilla et al. (2006) investigated the influence of grading on the behaviour of Italian silt by controlling its gradation using sedimentation to avoid significant alteration to the overall mineralogy. The study examined silt-clay mixtures with varying clay fractions of 45%, 25%, 8%, and 3.5%, with sand content ranging from 0 to 10%. The oedometer compression curves are reported in Figure 2.4. As the clay content decreases, both the loading and unloading curves become flatter. For the samples with 8% and 3.5% clay content, it is no longer possible to identify a distinct one-dimensional normal compression line (1D NCL). Undrained triaxial tests performed on mixtures with 45% clay content showed contractive behaviour as they approached the critical state, and as the clay content reduced, the dilative tail on the stress path grew (Fig. 2.5).

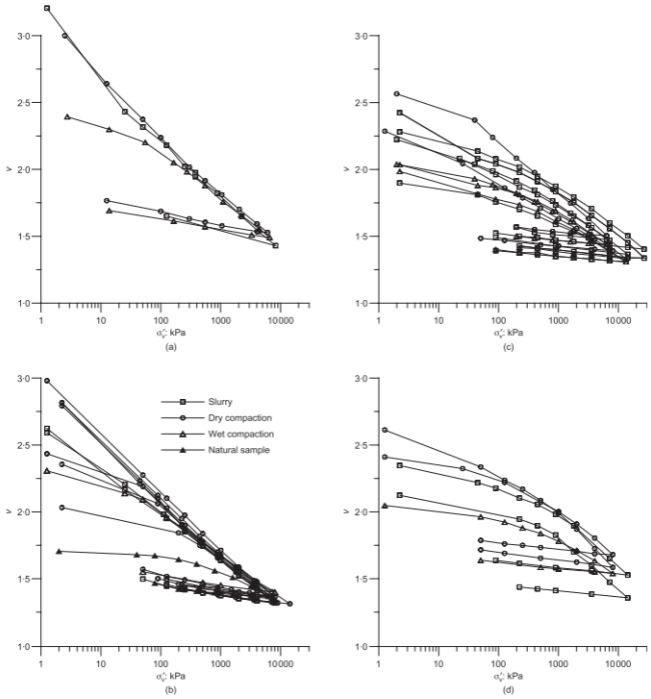

Figure 2.4: Oedometer compression curves: (a) 45% clay content; (b) 25% clay content; (c) 8% clay content; (d) 3.5% clay content - Nocilla et al. (2006)

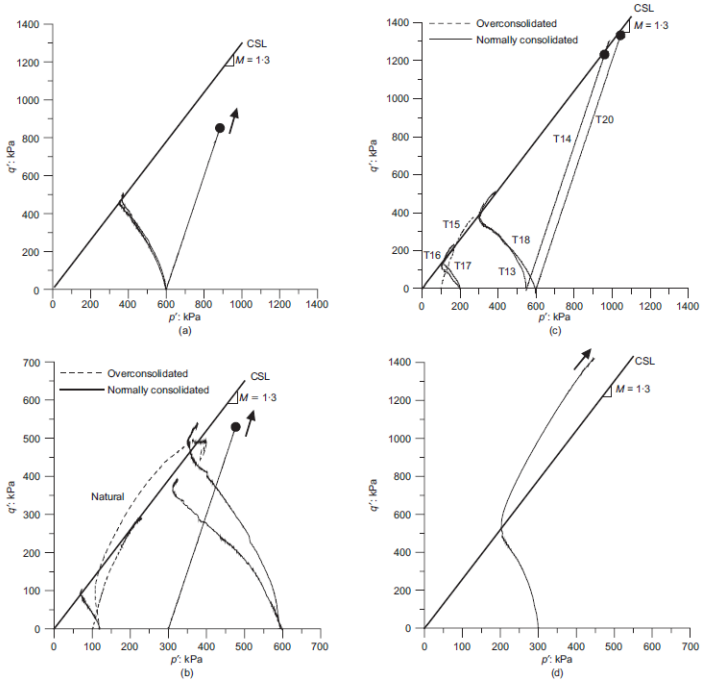

Figure 2.5: Stress paths during shearing: (a) 45% clay content; (b) 25% clay content; (c) 8% clay content; (d) 3.5% clay content (data points indicate critical states of drained tests or final state if test incomplete) - Nocilla et al. (2006)

Anantanasakul et al. (2012) presented the results of a series of laboratory tests performed on specimens with three different clay contents: 68%, 45%, and 24%. The base clay used in this study was kaolin, and the silt was made of ground quartz. The undrained shearing response was consistent with typical contractive behaviour, showing sharper increases and higher stress ratios with increasing silt content. However, as shown in Figure 2.6 the mixtures did not exhibit the transition between contractive and dilative behaviour observed in undrained triaxial compression tests by Cola and Simonini (2002) and Nocilla et al. (2006).

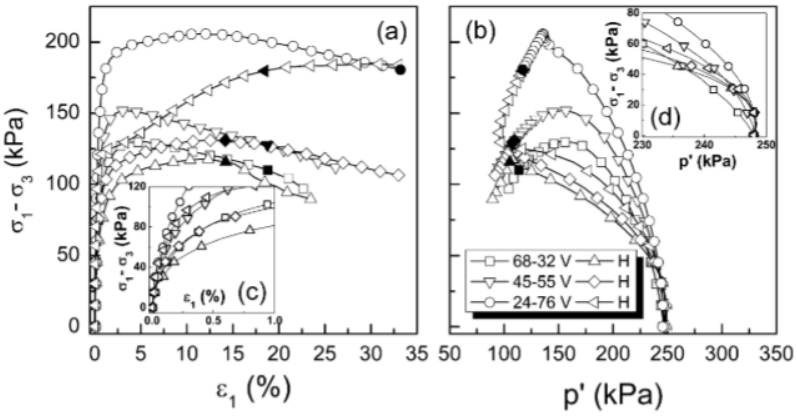

Figure 2.6: Results of undrained triaxial compression tests: (a) deviatoric stress versus axial strains; (b) effective stress paths; insets (c) and (d) show results at small vertical strains - Anantanasakul et al. (2012)

Studies on silty Venice lagoon soils by Cola and Simonini (2002) and silt-clay mixtures by Anantanasakul et al. (2012) show larger pore pressure changes with increased silt content during undrained shearing. This

finding contradicts the general perception that normally consolidated soil exhibits greater contractive tendancies during shear with higher clay contents. However, volumetric response in drained triaxial compression tests by Anantanasakul et al. (2012) show that the silt content does not have a significant influence on volume change behaviour.

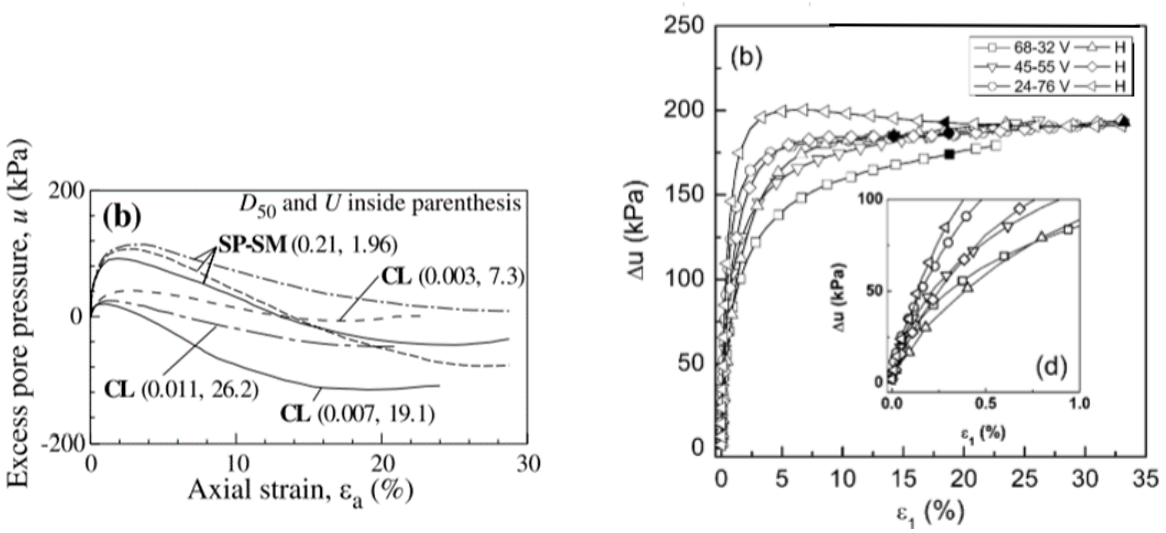

(a) (b)

Figure 2.7: Excess pore pressure response of undrained triaxial compression test (a) CL (30% clay, 45% silt, 25% sand) and SM (98% sand, 2% clay) soils tested by Cola and Simonini (2002), and (b) silt-clay mixtures with varying clay content (legend shows clay-silt ratio) tested by Anantanasakul et al. (2012)."

2.3 Microstructure of Compacted Soil

According to Mitchell (1976), the concepts of 'fabric' and 'structure' in soil mechanics are defined as follows:

"The term 'fabric' refers to the arrangement of particles, particle groups, and pore spaces in a soil. The term 'structure' is used by some interchangeably with the term 'fabric'. Herein, however, the term 'structure' is taken to have the broader meaning of the combined effects of fabric, composition, and interparticle forces."

Mitchell (1976) divides fabric into macrofabric and microfabric. Macrofabric, which includes voids, root holes, cracks, and compaction lift laminations, is generally more critical for natural soil shear strength than for compacted soil. Therefore, macrofabric will not be considered further. Microfabric considers the behaviour and orientation of individual soil particles or particle clusters, which will be covered in more detail.

To understand the microfabric of compacted soils, two prominent models are reviewed: the Particle Level Model and the Aggregate Model. The Particle Level Model, advanced by Lambe (1958), focuses on the interactions between soil water and individual particles. In contrast, the Aggregate Model, proposed by Barden and Sides (1970) and expanded by Hodek (1972), emphasises the role of particle clusters and their deformation under different moisture conditions.

2.3.1 Particle Level Model

Proctor (1933) developed theories on soil compaction mechanics, focusing on soil water interaction with particles. Lambe (1958) expanded this with colloidal and crystal chemistry, creating a model based on "water deficiency." This model distinguishes between double-layer water (attracted by soil particles) and free water (excess water).

- Below Optimum Moisture:
  Insufficient water and high electrolyte concentrations create a flocculated fabric due to depressed double layers and reduced interparticle repulsion.
- Optimum Moisture:
  The double layer expands, electrolyte concentration decreases, and "lubrication" occurs, leading to increased interparticle repulsion and a denser, more orderly particle arrangement.
- Above Optimum Moisture:
  The double layer continues to expand, increasing interparticle repulsion and creating a highly ordered particle arrangement. However, the compacted mass becomes less dense as water occupies more space.

Lambe's theory provided investigators with an adequate framework for understanding the mechanisms controlling compacted clay compressibility. However, compacted soil subjected to increasing applied stress, as in a laboratory test, or environmental changes, as in an embankment, experiences complex changes in the system variables that are difficult to measure and predict accurately.

2.3.2 Aggregate Model

Barden and Sides (1970) used scanning electron microscopy to develop an aggregate model of compacted soil fabric. Before compaction, the soil particles were clustered into visible aggregates of varying proportions. After compaction, significant differences were observed at low magnifications between soils compacted wet and dry of optimum moisture content (Fig. 2.8).

- Compacted dry of optimum:
  Distinct packets or domains remained visible, with large inter-aggregate pores intervening.
- Compacted wet of optimum:
  Individual domains and pores were no longer distinguishable, resulting in a more homogeneous structure.

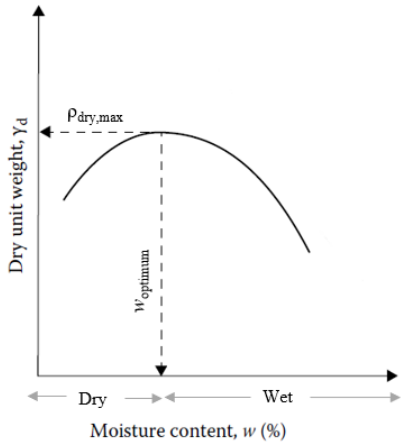

Figure 2.8: Moisture density curve - adapted from Das (2019)

Higher moisture contents weaken soil packets, allowing easier deformation under compaction, reducing large pore volumes, and resulting in a denser, more homogeneous structure. Hodek (1972) expanded the aggregate model by introducing "deformable aggregates," accounting for moisture-dependent strength and deformation behaviour. He incorporated the swelling behaviour of soil upon saturation, noting that aggregates compacted dry of optimum exhibited more swelling due to their larger initial pore spaces compared to those compacted wet of optimum. Hodek concluded that the aggregate model provided a superior explanation of compacted soil behaviour compared to the particle level model proposed by Lambe (1958).

2.3.3 Laboratory- and Field-Compacted Clayey Soils

Jommi and Sciotti (2002) investigated the microstructure of field- and laboratory-compacted clayey soil, performed by means of scanning electron microscopy (SEM) and mercury intrusion porosimetry (MIP). They observed differences in the microstructure of laboratory-compacted and field-compacted clays as suggested earlier by Barden and Sides (1970), even when compacted to similar dry density and water content. The differences were observed at all levels of particle organisation.

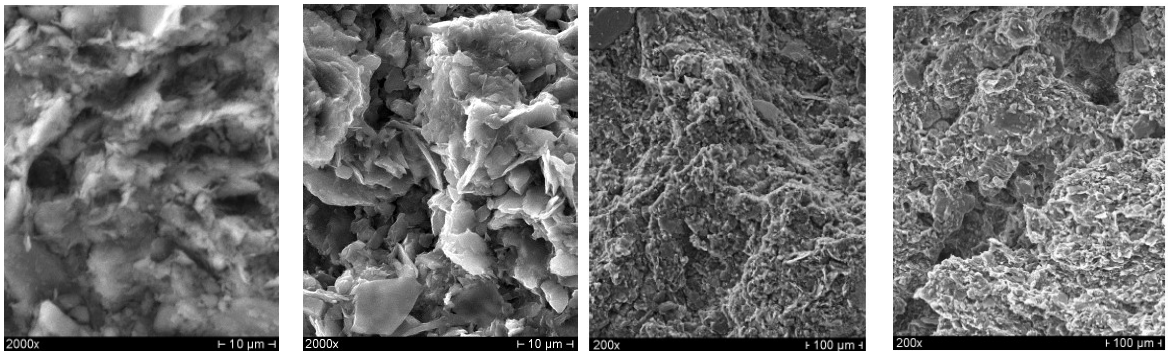

(a) (b) (c) (d)

Figure 2.9: Scanning electron microscope micrographs of (a) Laboratory compacted clay 2500x (b) Field compacted clay 2500x (c) Laboratory compacted clay 200x (d)Field compacted clay 200x - Jommi and Sciotti (2002)

1. Elementary Particle Arrangement:
   - In laboratory compacted clay, particles were not clearly identifiable (Fig. 2.9a), appearing coated and resulting in a partially discernible structure with mostly face-to-face or edge-to-face contacts at low angles.
   - In field compacted clay, particles were distinct with well-defined edges compared to laboratory samples, inter-particle contacts are edge-to-face or edge-to-edge arranged in a more random manner (Fig. 2.9b).
2. Particle Assemblages (Aggregates):
   - Aggregates in laboratory compacted clay were clearly distinguishable but smaller, with less pore space between them (Fig. 2.9c).
   - Aggregates in field compacted clay were larger (100-300 μm) and more irregular in shape, with larger and more irregular pore spaces (Fig. 2.9d). Some samples contained a matrix of clay and silt filling voids between aggregates.
3. Porosity:
   - Inter-aggregate pores were larger (30-80 μm) and more irregular in field-compacted samples compared to laboratory-compacted samples (up to tens of μm).
   - Intra-aggregate pores were more isometric and regular in field-compacted samples (1.5-5 μm) than in laboratory-compacted samples (2-6 μm). Field-compacted samples also showed matrix porosity (2-10 μm) not observed in laboratory samples.

These differences in microstructure have important implications for the mechanical and hydraulic behaviour of the clays. For example, the authors suggest that field-compacted clays exhibit a stiffer response and different hydraulic properties compared to laboratory-compacted clays. The authors suggest that these findings highlight the importance of carefully considering the differences between laboratory-compacted clays and field-compacted earthworks when using laboratory data as a reference for field applications.

2.4 Research Gap

A critical gap persists in the comprehensive characterisation of Dutch soils used in dike construction, particularly in their compacted state, which most accurately reflects in situ conditions. The current Dutch assessment standards, primarily derived from studies conducted in the 1980s, may not fully encompass the complexities and variations inherent in these specific soil types. In particular, these standards rely on limited soil characterisation tests (e.g., soil classification) that do not entirely capture the potential mechanical behavioural differences.

Furthermore, the majority of research investigating the influence of soil composition on mechanical behaviour has relied on controlled mixtures of manufactured soils (e.g., kaolin, clean sand), limiting the direct applicability of these findings to the diverse and naturally occurring soils found in the Netherlands. Although Nocilla et al. (2006) made significant progress by examining the impact of gradation on Italian silt, a comparable investigation specifically focused on local Dutch soils, particularly in their compacted state, remains absent from the literature.

This knowledge gap hinders the development of optimised dike construction methodologies that leverage readily available local materials and incorporate innovative, sustainable techniques. Additionally, it limits the understanding of the long-term performance of these structures under various anthropogenic and environmental stresses.

Chapter 3

Research Approach

This chapter presents the research methodology employed to investigate the mechanical behaviour of locally sourced Dutch clays and their potential in dike construction. Motivated by the research gap identified in the previous chapter, this chapter outlines the research questions and objectives, followed by the systematic approach adopted to address them.

3.1 Research Questions

To address the need for effective characterisation and utilisation of local soils in dike construction, this study focuses on the following research questions:

Main Question:
How does the mechanical behaviour of three compacted Dutch clays, with varying erodibility, differ under various loading conditions? What role does soil composition play in these observed behavioural differences?

Sub-questions:
Can soil mixing enhance the mechanical properties of unsuitable soils, thereby offering a feasible solution to existing dike construction practices?

Can a versatile constitutive framework, developed for natural silty soils, accurately capture the mechanical responses of compacted clay with varying compositions across different loading conditions?

3.2 Research Objective

This research aims to characterise the mechanical behaviour of three types of locally sourced Dutch clay in their compacted state, each categorised by varying levels of erodibility to determine their suitability for dike construction. Through a detailed experimental investigation focused on characterising their compression and shear behaviour, the study will reveal how soil composition influences engineering properties. Additionally, the study will evaluate the capabilities of a recently developed constitutive model, originally designed for natural silty clay, in reproducing the behaviour of these compacted soils. This assessment will involve simulating laboratory tests to evaluate the model's ability to capture the behavioural features observed. By examining how the varying composition across the three soil types is reflected in the model parameters, the study will broaden the predictive model applicability for a wider range of soil types encountered in geotechnical engineering projects.

3.3 Methodology

To answer the research questions and fulfil the research objectives, this study will employ an experimental and numerical research methodology. This process will begin with the careful selection of materials based on their relevance to the study objectives, followed by an experimental campaign to characterise their mechanical properties and behaviour. Finally, the laboratory data will be utilised to calibrate and validate a constitutive model. A flowchart outlining the methodology is presented in Figure 3.3

3.3.1 Material Sourcing

The material used in this study was sourced from the Lingemeer area in the Netherlands, provided by Delgromij, a company specialising in combining natural resource extraction with sustainable area development. This area shown in Figure 3.1, formerly used for agriculture, has been transformed into a recreational landscape (Fig. 3.1).

The materials were classified based on their erosion resistance according to Dutch standards (Table 2.1):

- Material type I: Classified as clay with high erosion resistance.
- Material type II: An intermediate material, on the borderline of being classified as having moderate or high erosion resistance. Notably, type II meets the minimum requirements for suitability in dike construction.
- Material type III: Classified as clay with low erosion resistance.

The material was supplied in sealed buckets, and to reduce bio-degradation, it was stored in a climate-controlled room at 10 ± 1°C and 90% relative humidity.

To assess the potential of soil mixing for optimising existing dike construction practices, three sets of mixtures using material types I and III at dry mass ratios of 1:4, 1:1, and 4:1 (type I to type III) will be prepared. The erodibility and composition of each mixture will be determined according to relevant Dutch standards to identify which mixture most closely resembles the properties of material type II, the benchmark material that satisfies the minimum requirements for dike construction.

(a) (b)

Figure 3.1: Material extraction in Lingemeer - (a) 2012 to (b) 2024

3.3.2 Experimental Approach

A laboratory testing program consisting of three phases was designed; soil characterisation, fabric identification and mechanical testing.

Soil Characterisation

Soil composition was assessed by determining the particle size distribution and organic content. Index tests were performed to determine the liquid and plastic limits as they provide insights into fine-grained soil behaviour (Wood, 2014a). These assessments are crucial for understanding the fundamental properties of the soils being studied, in addition to them being integrated into Dutch standards for evaluating erosion resistance (Chapter 2). Compaction tests were conducted to determine the maximum dry density and optimum moisture content, as these represent the target compaction characteristics for soils in dikes.

Fabric identification

To understand how the compositional and compaction characteristics translate into the soil microstructure, Environmental Scanning Electron Microscopy (ESEM) was employed. The analysis was focused on how varying soil compositions influenced particle arrangement, pore size distribution, and aggregate formation. The microstructural features were then analysed and linked to the observed macroscopic behaviour that impacts the overall performance of the compacted clay.

Mechanical Testing

The mechanical behaviour was investigated through a series of oedometer and triaxial tests on laboratory-compacted specimens prepared at their optimum moisture content to achieve maximum dry density.

Incremental loading oedometer tests were conducted to assess the one-dimensional compression behaviour of the compacted clay. The oedometer tests were continued to a maximum vertical effective stress significantly exceeding that typically encountered in a dike. Drained and undrained triaxial compression tests were conducted to evaluate the pre-failure compression and shear responses of the soils under varying stress levels and states, replicating those experienced in both normally consolidated and overconsolidated field conditions. The stress levels in the triaxial tests were designed to encompass stress levels representative of in situ conditions while remaining within the controllable range of the laboratory setup. The stress paths explored by combining the oedometer and triaxial tests provide a representation of the soil stress state in a dike during raising and in the active shear zone of a dike slope slip surface, as depicted in Figure 3.2.

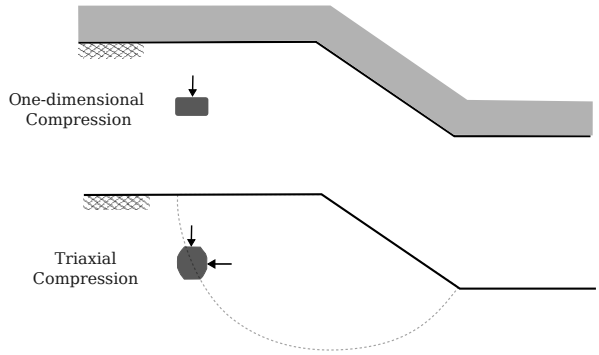

Figure 3.2: Representative soil stress-states beneath an embankment

The deformational responses from the mechanical tests were thoroughly analysed to draw conclusions on the behavioural differences across the three material types and to derive input parameters used to calibrate the constitutive model.

3.3.3 Constitutive Modelling

A recently developed constitutive model for natural silty clay (Chao, 2024) will be utilised to simulate the experimental results obtained for material types I and III. The model parameters will be calibrated based on the experimental data from these two materials to capture their compression and shear response. Subsequently, the predictive accuracy of the calibrated model will be assessed by simulating the laboratory tests on material type II, a soil with intermediate properties, and comparing the simulation results with the corresponding experimental data. This approach aims to validate the model's ability to work beyond its calibration dataset and predict the behaviour of soils with properties not explicitly included in the calibration process. A constitutive model that accurately replicates the behaviour of soils across a range of

compositions is essential for predicting the performance and stability of geotechnical structures under various loading conditions, ultimately informing safe and efficient design practices.

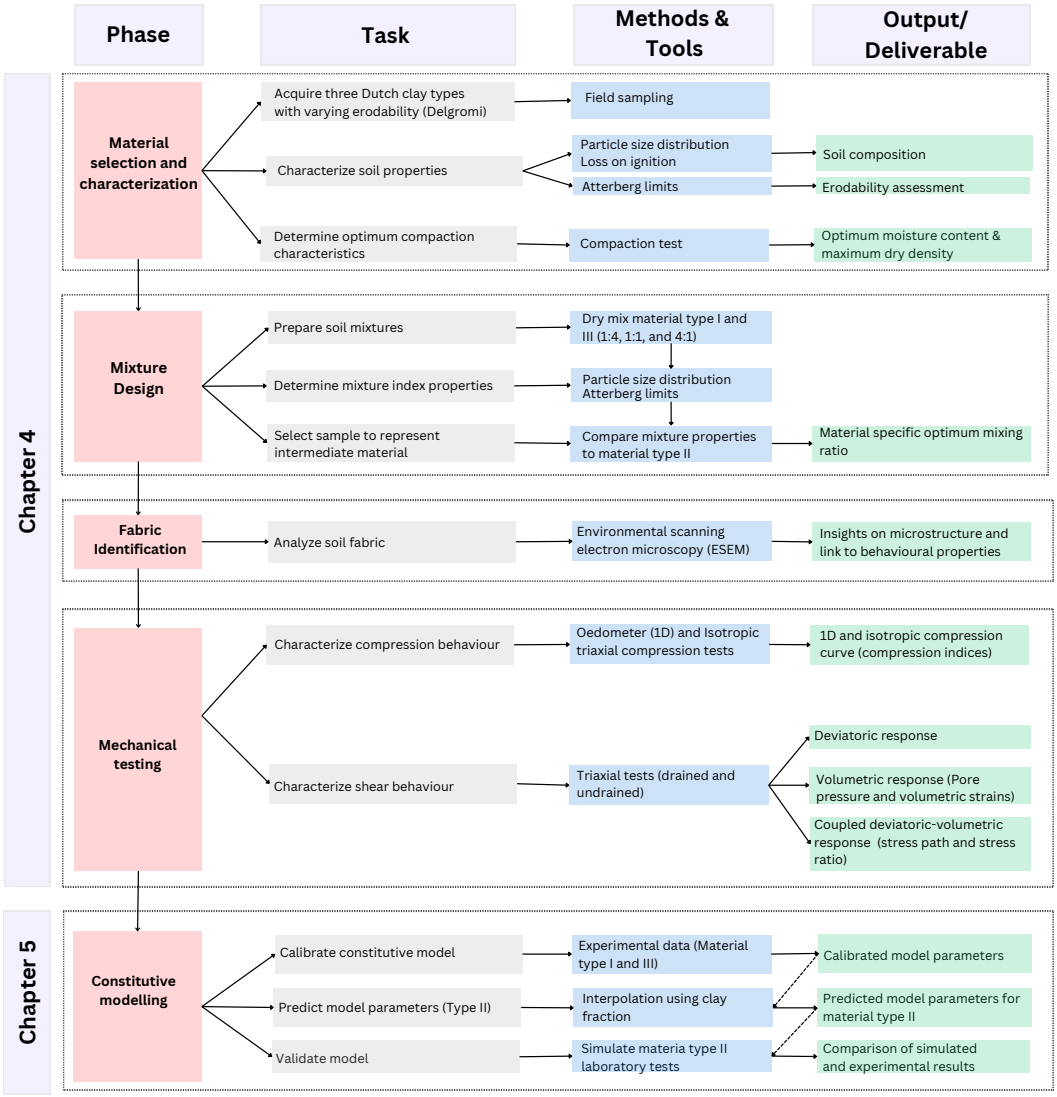

Figure 3.3: Methodology Flowchart: Overview of Phases, Tasks, Methods & Tools, and Outputs or Deliverables for the Study

Chapter 4

Experimental Study & Results

This chapter presents the results of the experimental campaign outlined in Chapter 3, which was designed to evaluate the mechanical behaviour of soils and the influence of varying compositions on their suitability in the application of dike reinforcement. The chapter begins with a detailed characterisation of the soil properties (i.e., composition, Atterberg limits, and compaction), followed by a micro-structural analysis of the soil fabric using Environmental Scanning Electron Microscopy (ESEM). Finally, the mechanical testing procedures (i.e., oedometer and triaxial) are detailed, and an analysis of compression and shear behaviour is presented. This analysis highlights the variations observed across the tested materials and their implications for the design of effective soil reinforcement strategies.

4.1 Soil Characterisation

Soil characterisation tests were performed on the three materials as a first step in this experimental campaign to establish a baseline understanding of the fundamental properties of each material. The results, summarised in Table 4.1, are essential for interpreting the mechanical behaviour observed in the subsequent testing phases.

Table 4.1: Index properties of the tested materials

Index properties	Type I	Type II	Type III
Sand content (%)	20	29	46
Silt fraction (%)	38	38	31
Clay content (%)	42	34	23
Loss on ignition (%)	5.74	5.23	3.88
Liquid limit, w_l (%)	60.5	45.5	32.8
Plasticity index, I_p (%)	34.8	23.0	15.6
Maximum dry density, $\rho_{d,max}$ (kg/m^3)	1610	1701	1791
Optimum water content, w_{opt} (%)	19.0	17.5	16.0
Specific gravity, G_s (-)	2.551	2.557	2.621

4.1.1 Soil Composition

Particle size distribution was determined using wet sieving for the fraction of soil greater than 63 μm, and the hydrometer for the finer fraction (BS1377, 1996). Figure 4.1 reports the particle size distribution of the three material types. The soil composition across the three types varies from sandy to clayey, with a consistent silt content throughout. The material ranges from sandy to silty clay.

In addition to the base materials, the particle size distribution of the three laboratory-prepared mixtures is shown in Figure 4.1, and the soil fractions are reported in Table 4.2. The denoted ratio is the dry mass ratio of material type I to III. Among the mixtures, Mix II (1:1) most closely resembles the overall distribution of the intermediate material type II, particularly in its clay content, which matches the 34% of type II. Additionally, Mix III (4:1), has the most similar fine content, 75% compared to 71% of type II.

The organic content, determined by igniting oven-dried samples in a furnace at 440^{o}C (ASTM D2974-14, 2014), varies between 5.7% and 3.9% across the three tested materials as shown in Table 4.1. The Dutch standards presented in Chapter 2 specify the organic content requirement as determined from hydrogen peroxide treatment but this study employed the loss on ignition as a measure of the organic content.

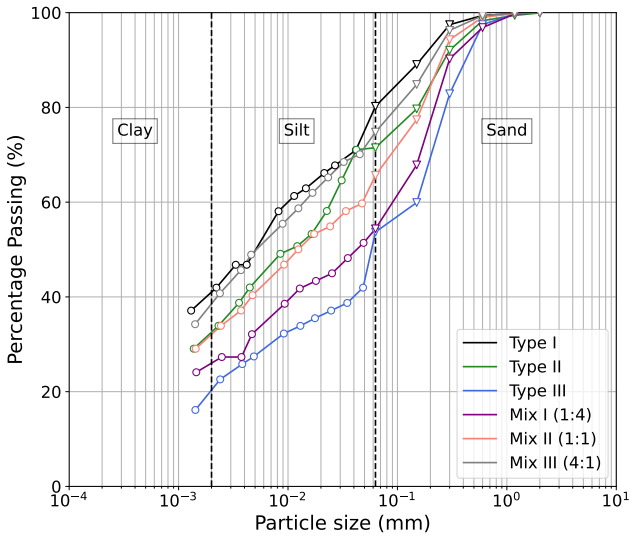

Figure 4.1: Particle size distribution of the tested materials

4.1.2 Atterberg Limits

The Atterberg limits were determined for soil from which material retained on a 425 μm test sieve had been removed. The liquid limit was measured using the 80g/30° cone penetrometer (BS1377, 1996). The erodibility assessment of the three material types and mixtures is presented in Figure 4.2.

To evaluate the impact of the drying temperature on soil plasticity, the Atterberg limits were determined after drying the soil at 100°C and 60°C. As shown in Figure 4.2, drying at 100°C reduced the liquid limit and plastic limit by 30% and 23%, respectively. This assessment was conducted on material type I, which has the highest clay content. Numerous studies have investigated how drying methods affect the engineering properties of clay. The observed reduction in plasticity can be attributed to increased particle aggregation at higher drying temperatures (Basma et al., 1994). According to Mitchell (1976), natural clay predominantly contains divalent calcium and magnesium ions, with less common monovalent sodium and potassium ions. Divalent cations create stronger inter-particle attractions compared to monovalent cations. At higher drying temperatures, the concentration of pore salts is increased by removing free and bound water, enhancing inter-particle attractions and reducing particle separation. The resulting increased capillary stresses cause closer particle contact and the formation of strong bonds. This aggregation decreases the specific surface area available for water interaction, thereby lowering the liquid limit and plasticity index. Based on the above findings, lower drying temperatures, ranging from 40°C to 60°C, were adopted throughout the experimental study.

Figure 4.2 shows the erosion classification of the three tested mixtures. According to the Dutch classification method, the Mix II (1:1) and Mix III (4:1) are categorised as erosion-resistant clay, with Mix II (1:1) beign on the borderline between erosion resistant and moderately erosion resistant. Mix II (4:1) closely aligns with the properties of the intermediate material, type II, in terms of erodibility, as reflected by its position on the plasticity chart. Considering the particle size distribution of the mixtures discussed in Section 4.1.1, these findings suggest that the fines content (i.e., silt and clay) contributes to the soil erosion resistance, rather than the clay content alone.

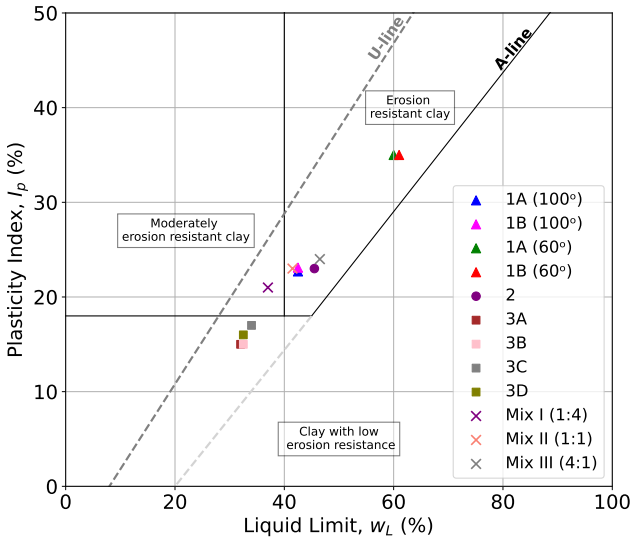

Figure 4.2: Plasticity chart with test results for classifying erosion Resistance

Table 4.2: Index properties of the laboratory-prepared mixtures

Index properties	Mix I (1:4)	Mix II (1:1)	Mix III (4:1)
Sand content (%)	46	34	25
Silt fraction (%)	27	32	34
Clay content (%)	27	34	41
Liquid limit, w_l (%)	37.0	41.5	46.5
Plasticity index, I_p (%)	20.5	23.2	24.0

4.1.3 Compaction Test

The compaction tests were conducted using Standard Effort (12,400 $ft-lbf/ft^3$ (600 kN-m/m3) for material types I and III. Due to material availability, the compaction test was not performed on type II. Instead, the optimum moisture content and dry density for type II were interpolated between those of types I and III, based on the reasonable assumption that properties of type II would fall within the range defined by these extremes. The moisture density curves are reported in Figure 4.3.

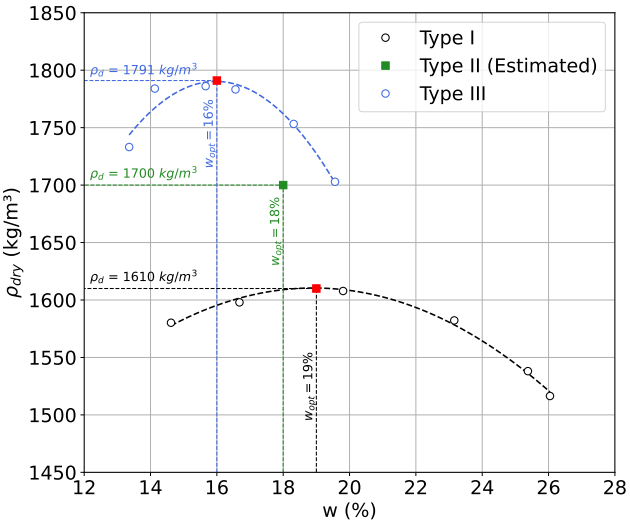

Figure 4.3: Soil moisture-density relationships from Standard Proctor

4.2 Fabric Identification

The microstructure of the compacted soil samples was examined using Environmental Scanning Electron Microscope (ESEM) micrographs. Specimens were prepared by freeze-drying with liquid nitrogen and breaking the sub-samples to achieve a natural yet relatively flat surface. All micrographs were taken from vertical sections at magnifications ranging from 100x to 2500x.

Figure 4.4 presents very low magnification (x125) micrographs of compacted samples of material types I and III, illustrating their overall structural differences. Figure 4.4a displays a denser, more massive structure with fewer voids, while Figure 4.4b shows a looser structure with more distinct granular aggregations.

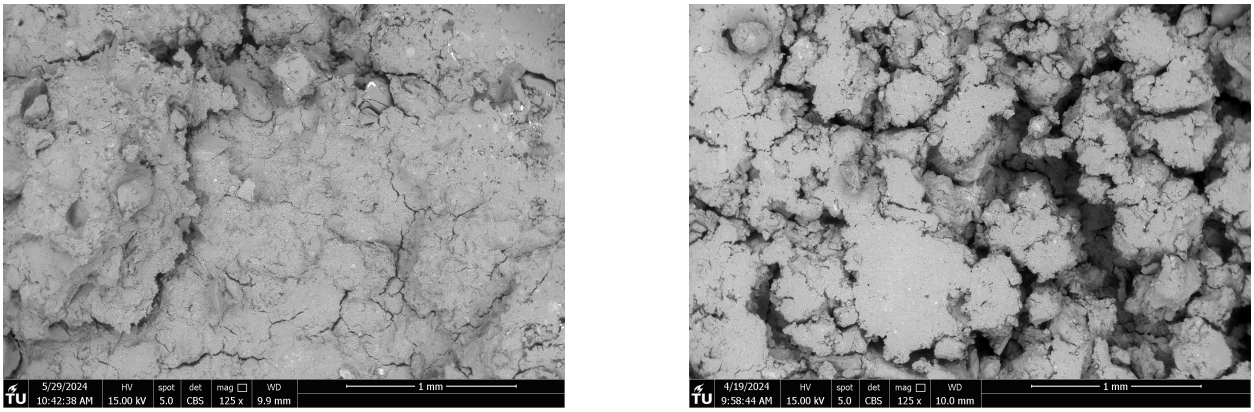

(a) (b)

Figure 4.4: ESEM micrographs showing overall structure (125x) on compacted samples of material (a) Type I (b) Type III

The observed fabric is a product of the laboratory compaction and inherent soil composition (particle size distribution, organic content, mineralogy, etc.) The description of the microstructure will follow the approach proposed by Collins and McGown (1974) for natural clay and will be linked to behavioural characteristics that impact the overall performance of the compacted clay. The features are divided into two types:

1. **Elementary Particle Arrangements**

   These consist of single forms of particle interaction at the level of individual clay, silt, or sand particles, or interactions between small groups of clay platelets or clothed silt and sand particles. High magnification (2500x) ESEM imaging was used to examine these elementary arrangements, however, clear inter-particle interactions may be less distinguishable in laboratory compacted clays due to the dense packing.

   - **Material type I & II:** The high magnification images (Fig. 4.5a & 4.5b) show densely packed and closely arranged clay particles. The high density of clay particles results in smaller visible pore space, with a more intact structure where the clay platelets interact to form connectors between the sand and silt particles.
   - **Material type III:** The images reveal a more loosely packed arrangement with visible larger inter-aggregate pores (Fig. 4.5c). The clay and silt particles appear to form fewer clusters, where the clay particles partially coat the silt and sand particles, leading to a more open structure compared to Type I and II.

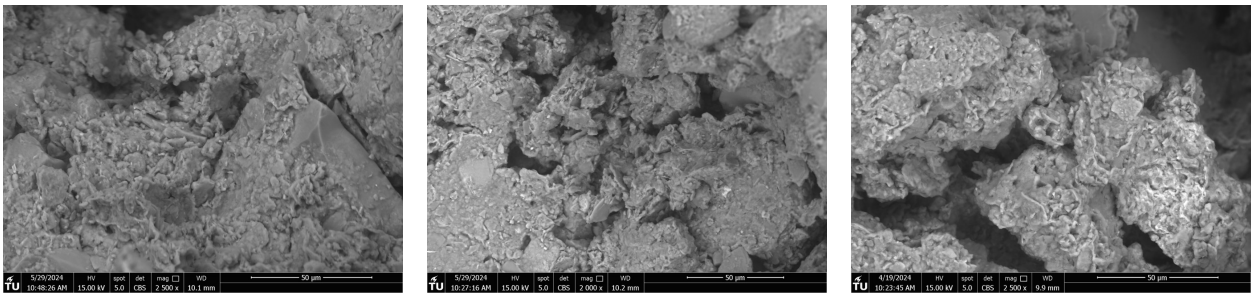

(a) (b) (c)

Figure 4.5: ESEM micrographs (2500x) on compacted samples of material (a) Type I (b) Type II (c) Type III

2. **Particle Assemblages**

   These are units of particle organisation with definable physical boundaries and consist of one or more forms of elementary particle arrangements or smaller particle assemblages. Low magnification (500x) ESEM images were used to identify these assemblages. During sample preparation and imaging, the soil was subject to brief drying of which the effects can be visible and could be linked to the materials susceptibility to degradation.

   - **Material type I & II:** The fabric is organised in large aggregates with size greater than 300 μm (Fig. 4.6a & 4.6b). The visible voids ranging from 50 to 70 μm could be attributed to shrinkage due to drying, which is more pronounced at higher clay content. The large aggregates are tightly bound, reflecting the nature of clay particles which contribute to creating a compact dense and massive structure.
   - **Material type III:** The aggregates in the low magnification image have dimensions ranging from approximately 100 μm to 300 μm (Fig. 4.6c). The fabric is characterised by a more granular appearance with aggregates less compact due to the higher sand content, leading to larger and more irregularly shaped assemblages. The boundaries between these assemblages are more distinct and do not resemble the cracks observed in material types I and II.

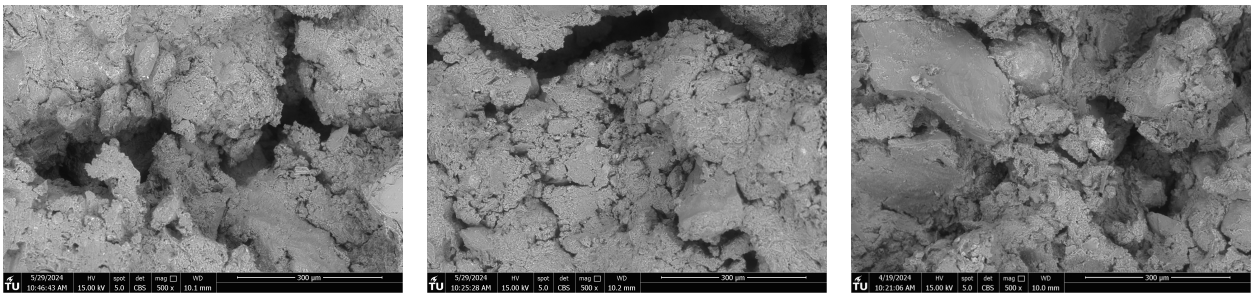

(a) (b) (c)

Figure 4.6: ESEM micrographs (500x) on compacted samples of material (a) Type I (b) Type II (c) Type III

Overall, the ESEM micrographs support the classification of material type I as clay with high erosion resistance, given its dense structure with smaller pores. This type of microstructure is expected to have low hydraulic conductivity, making it suitable for applications in dike construction where resistance to erosion and water flow is crucial. However, the observed shrinkage cracks in material types I and II imply that these materials are more susceptible to degradation upon drying compared to material type III, where the microstructure exhibited higher resilience to drying during preparation and imaging. Notably, when assessing the suitability of the intermediate material type II, its microstructure closely resembles that of type I, suggesting its potential suitability for dike construction.

4.3 Mechanical Tests

Having established the fundamental properties of the materials and gained insights into their microstructural characteristics, the experimental campaign proceeded to investigate their mechanical behaviour. This section details the mechanical testing program, including sample preparation, triaxial tests, and oedometer tests. The results of these tests will be analysed to characterise the material response in terms of compression and shear.

A comparative analysis of the results will shed light on how these materials, with different suitability for dike construction, perform under similar loading conditions, informing their potential use in geotechnical engineering applications.

4.3.1 Sample Preparation

To ensure consistency across all tests, the following standardised procedure was followed for preparing samples for mechanical testing:

1. Wet soil was dried at 40°C and then crushed using a mortar and pestle.
2. The soil was mixed with demineralised water to the predetermined optimum moisture content (Figure 4.3), stored in a polyethene bag, and cured for 24 hours in a climate-controlled room at 10 ± 1°C and 90% relative humidity.
3. Soil was compacted through impact compaction in three layers in a 101.6 mm diameter mould with a 24.5 N hammer dropped from a height of 305 mm producing a compactive effort of 600 kN-m/m3. The compacted soil was left to rest for 24 hours.
4. The compacted sample was extruded using a screw jack. Thin-walled stainless steel tubes (for triaxial test sample) or the oedometer ring were carefully pressed into the compacted sample using the screw

jack. To accommodate the volume displaced by the advancing sampling tube, the surrounding soil was simultaneously trimmed to allow for lateral expansion while avoiding crack propagation.

When the dry soil was mixed with water, it had a tendency to form clumps. These clumps were more pronounced in samples of material types I and II compared to III due to their higher clay content, as seen in Figures 4.7 and 4.8 obtained from medical CT scans. The mixed soil was then allowed to cure for 24 hours to ensure uniform moisture distribution. However, some clumps remained visible after compaction, particularly at the bottom of each compaction layer (Figures 4.7a to 4.7c).

The CT scans of the trimmed triaxial samples (Figures 4.7d to 4.7f) indicate that the trimming and extrusion processes further densified the soil, particularly in the lower regions of the trimmed sample. A similar trimming procedure was adopted by Johnson and Purdue (1979).

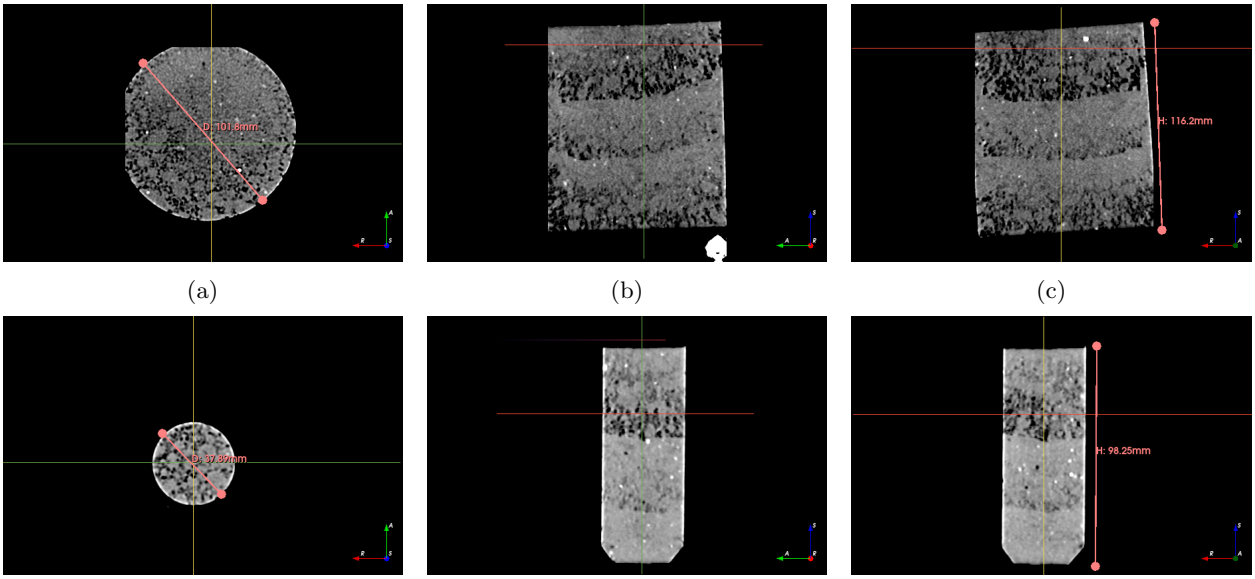

(a) (b) (c)

(d) (e) (f)

Figure 4.7: Sample TX-2A: Compacted sample (a) X-Y plane; (b) X-Z plane; (c) Y-Z plane; Trimmed sample (d) X-Y plane; (e) X-Z plane; (f) Y-Z plane

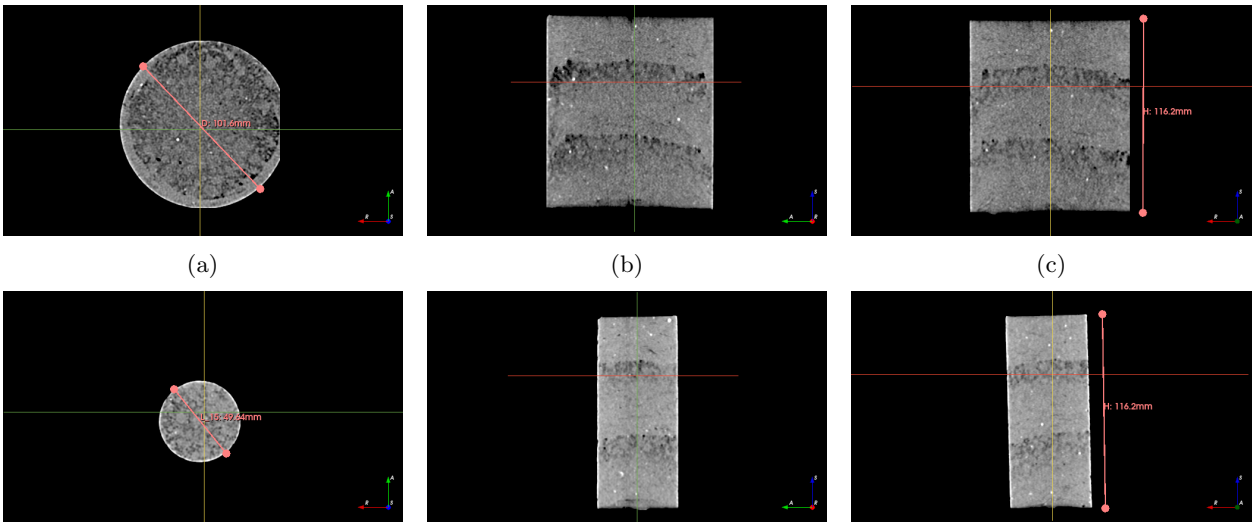

(a) (b) (c)

(d) (e) (f)

Figure 4.8: Sample TX-3C: Compacted sample (a) X-Y plane; (b) X-Z plane; (c) Y-Z plane; Trimmed sample (d) X-Y plane; (e) X-Z plane; (f) Y-Z plane

Table 4.3 presents the properties of the prepared test samples and their compaction characteristics. The parameters include the initial height (H_0), initial diameter (D_0), initial water content (w_i), dry density (ρ_d), relative compaction as a percentage of the maximum dry density determined in Section 4.1.3 ($\rho_{d,max}$), and initial degree of saturation (S_{ri}).

Table 4.3: Prepared test sample properties and compaction characteristics

Type	Sample ID	H_0 (mm)	D_0 (mm)	w_i (%)	ρ_d (kg/m^3)	% of $\rho_{d,max}$ (%)	S_{ri} (%)
I	TX-1A	75.51	37.73	20.14	1653.40	103	94.6
	TX-1B	85.68	37.76	20.04	1642.26	102	92.3
	OED-1	19.03	49.99	20.14	1640.79	102	92.5
II	TX-2A	86.38	37.91	19.05	1668.13	98	91.4
	TX-2B	86.32	37.89	19.16	1679.20	99	93.7
	OED-2	19.04	50.03	18.45	1643.06	97	84.8
III	TX-3A	101.60	49.84	16.64	1770.10	99	90.7
	TX-3B	101.35	49.64	17.15	1763.84	98	92.5
	TX-3C	102.16	49.68	16.63	1774.70	99	91.4
	OED-3	19.03	49.99	16.16	1788.75	100	91.0

It is important to note that the use of demineralised water in sample preparation serves as a standardisation measure, ensuring consistency, comparability, and repeatability of experimental procedures, though it may not fully reflect the real in situ conditions of soil exposed to atmospheric interaction. It also creates a controlled environment, where changes in soil behaviour are attributed to the soil itself, free from external ion influence. The lack of minerals in demineralised water, however, may promote clay particle dispersion due to insufficient buffering capacity, unlike tap water, which can facilitate flocculation and particle aggregation. To assess the material sensitivity to water type, pH measurements were taken in both tap and demineralised water. The results presented in Table 4.4 show consistent pH, suggesting the soil has a high

buffering capacity. It is worth mentioning that during measuring the pH, after stirring, the soil-tap water suspension was less turbid than the soil-demineralised water suspension (Fig. 4.9), indicating that mineral deficiency in the latter promotes dispersion of the particles.

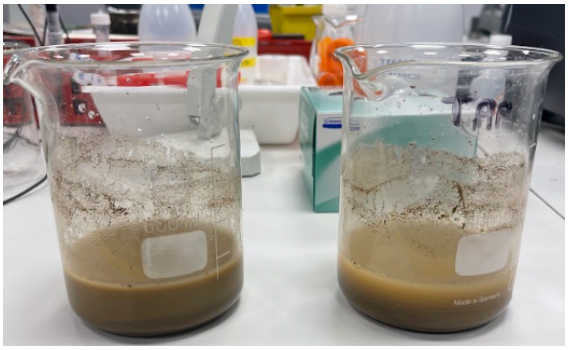

Figure 4.9: Material type I suspension in demineralised water (left) and tap water (right)

Table 4.4: Soil PH measurements

Sample	pH (Water)	pH (Water + Soil)
Demineralised water	6.70	7.00
Tap water	8.06	6.96

4.3.2 Triaxial Tests

Set-up and Specification

A series of triaxial compression tests were performed on isotropically consolidated samples, both undrained (TxICU) and drained (TxICD), to investigate the response to various stress paths and histories. Following saturation, samples were isotropically compressed at 8-11 kPa/day, a rate slow enough to prevent excess pore pressure generation. Undrained shearing was performed at a controlled axial strain rate of 0.015 %/min to assure pore pressure equalisation (Lade, 2016), and drained shearing was performed at a controlled axial stress of 8 kPa/day to avoid pore pressure accumulation.

A GDS triaxial apparatus was used, equipped with back pressure and cell pressure volume controllers, a pore pressure transducer, a 1 kN submersible load cell, and an LVDT. Lateral filter paper was used to facilitate drainage, and the sample was enclosed in a latex membrane with a suction cap ensuring good contact with the top cap and load cell.

Table 4.5 summarises key parameters: clay content, initial void ratio (e_i); void ratio after saturation ($e_{i,sat}$); imposed pre-consolidation mean effective stress ($p'_{c,TX}$); and the mean effective stress prior to shearing ($p'_{s,TX}$). It should be noted that the calculated overconsolidation ratio (OCR), defined as $p'_{c,TX}/p'_{s,TX}$, reflects the stress history imposed during the triaxial test itself and does not account for compaction stresses induced during sample preparation.

Table 4.5: Initial state and test specification

Type	Clay Content (%)	Sample ID	e_i (-)	$e_{i,sat}$ (-)	$p'_{c,TX}$ (kPa)	$p'_{s,TX}$ (kPa)	OCR (-)
I	42	TX-1A	0.543	0.723	115.4	113.3	1.0
		TX-1B	0.554	0.731	60.3	41.8	1.4
II	34	TX-2A	0.533	0.696	60.4	41.5	1.5
		TX-2B	0.523	0.681	116.1	113.2	1.0
III	23	TX-3A	0.481	0.511	59.6	40.8	1.5
		TX-3B	0.486	0.525	115.6	114.7	1.0
		TX-3C	0.487	0.527	42.0	41.2	1.0

Saturation

Compaction typically leaves the soil in a partially saturated state, as air cannot be fully expelled from the pore spaces (Johnson & Purdue, 1979). The process of saturating compacted clay specimens does not occur quickly and requires relatively high back pressures even for specimens compacted on the wet side of optimum (VandenBerge et al., 2014). Upon wetting, unsaturated samples tend to swell, with the degree of swelling depending on the clay mineralogy, initial compaction conditions, and confining pressure (Ladd, 1960). A consistent saturation procedure was followed for all the specimens to ensure uniformity. Specimens underwent back pressure saturation at 500-600 kPa over two to three days, under an average effective confining stress of 5-11 kPa (computed as the difference between applied cell and back pressure). The resulting volumetric strain due to swelling ranged from 10-12% in samples of material type I and II, and 2-3% in samples of type III, with the difference attributed to the difference in clay content.

Test Data Interpretation

The experimental data are interpreted in terms of mean effective stress (p'), deviatoric stress (q), volumetric strain (ϵ_p), and deviatoric strain (ϵ_q). These are derived from the raw data collected for each test using Equations 4.1 to 4.7. The following corrections were made to the experimental data:

1. Standard area correction assuming that the sample deforms as a right equivalent cylinder.
2. Radial stress correction due to initial confining pressure of the membrane, $\Delta\sigma_r^{(1)}$ (Rochelle et al., 1988).
3. Radial stress correction due to membrane stretching during the test, $\Delta\sigma_r^{(2)}$ (Fukushima & Tatsuoka, 1984).

The stress variables p' and q are computed as follows:

$$p' = \frac{\sigma'_a + 2\sigma'_r}{3} \tag{4.1}$$

$$q = \sigma'_a - \sigma'_r \tag{4.2}$$

$$\sigma'_a = \sigma_c + \frac{P_a}{A} - u_w \tag{4.3}$$

$$\sigma'_r = \sigma_c - u_w + \Delta\sigma_r^{(1)} + \Delta\sigma_r^{(2)} \tag{4.4}$$

Where:

σ'_a : Effective axial stress
σ'_r : Effective radial stress
σ_c : Cell pressure measured by cell pressure volume controller
P_a : Axial load measured by the load cell
A : Current sample area
u_w : Pore water pressure

Note: Compressive stresses and strains are assumed positive in this study.

The deviatoric strain ε_q is computed from the axial and volumetric strains as follows:

$$\varepsilon_q = \frac{2}{3}(\varepsilon_a - \varepsilon_r) = \varepsilon_a - \frac{\varepsilon_p}{3} \tag{4.5}$$

$$\varepsilon_a = -\ln \frac{H}{H_0} \tag{4.6}$$

$$\varepsilon_p = -\ln \frac{V}{V_0} \tag{4.7}$$

Where:

ε_a : True axial strain
ε_r : True radial strain
ε_p : True volumetric strain
H_0 : Initial sample height
H : Current sample height computed using the LVDT measurements
V_0 : Initial sample volume
V : Current sample volume computed using back pressure volume controller measurements

4.3.3 Oedometer Tests

The testing program involved three incremental loading oedometer tests performed using a traditional lever arm-weight type loading system. Oedometer rings with a diameter of 50 mm and a height of 20 mm were used, and they were lubricated to minimise side friction. Two porous stones were placed at the top and bottom of the sample to facilitate pore fluid dissipation. Following the loading pad adjustment, the saturation procedure involved filling the consolidation cell with water and allowing it to rest for 48 hours while recording the height change due to swelling. The vertical effective stress was incrementally increased to $\sigma'_{v,max}$ and then reduced to $\sigma'_{v,i}$ (Table 4.6) before removing the sample from the cell. Each load increment was maintained for at least 24 hours. Axial displacement was measured using a Linear Variable Displacement Transducer (LVDT).

Table 4.6: Oedometer test initial state specifications

Type	Clay Content (%)	Sample ID	e_i (-)	$e_{i,sat}$ (-)	$\sigma'_{v,i}$ (kPa)	$\sigma'_{v,max}$ (kPa)
I	42	OED-1	0.555	0.560	0.93	638.4
II	34	OED-2	0.556	0.584	1.04	635.0
III	23	OED-3	0.465	0.483	0.94	635.0

4.3.4 Compression Behaviour

The one-dimensional and isotropic compression responses of compacted materials are analysed to identify the effect of the clay content on compression behaviour. The relationship will be compared to established correlations in the literature for natural and reconstituted silty clay. The results are used to derive key parameters essential for calibrating the constitutive model.

Compressibility

The one-dimensional virgin compression lines (1D-VCL), presented in Figure 4.10, provide insights into how the clay content influences the material compressibility. The slope of 1D-VCL (C_c), increases from 0.107 for 23% clay content to 0.193 for 42% clay content. Similarly, the slope of the unloading-reloading line (1D-URL), known as the re-compression index (C_s), increases from 0.020 for 23% clay content to 0.039 for 43% clay content. The ratio of C_c to C_s ranges between 5 and 6. The slope of the isotropic normal compression line (ISO-NCL) and unloading-reloading (ISO-URL) line vary similarly with the clay content. The results are reported in Table 4.7, and the variation with clay content is depicted in Figure 4.11.

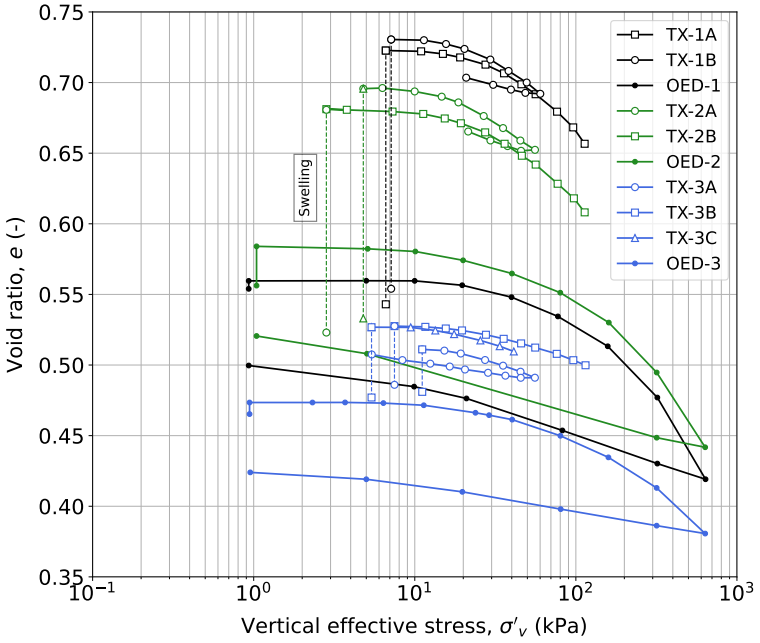

Figure 4.10: Compression response from isotropic and 1D compression

As shown in Figure 4.11, the slope of the 1D-VCL line is higher than the slope of the ISO-NCL across the three tested materials. Aside from the tested stress level (i.e., triaxial tests attained a stress level lower than oedometer tests) and the directional behaviour of soil, this difference could also be attributed to the varying degrees of swelling observed during the saturation stage of triaxial and oedometer tests. Triaxial test samples experienced significant swelling, with volumetric strains ranging from 10.0% to 12.0% for material types I and II, and between 2.0% and 3.0% for type III. In contrast, oedometer test samples swelled by only 0.3%, 1.2%, and 0.5% for material types I, II, and III, respectively. The change in void ratio due to swelling during saturation is depicted in Figure 4.10 with a dotted line, connecting the initial void ratio at the start of saturation to the void ratio at the end of saturation and beginning of isotropic and 1D compression.

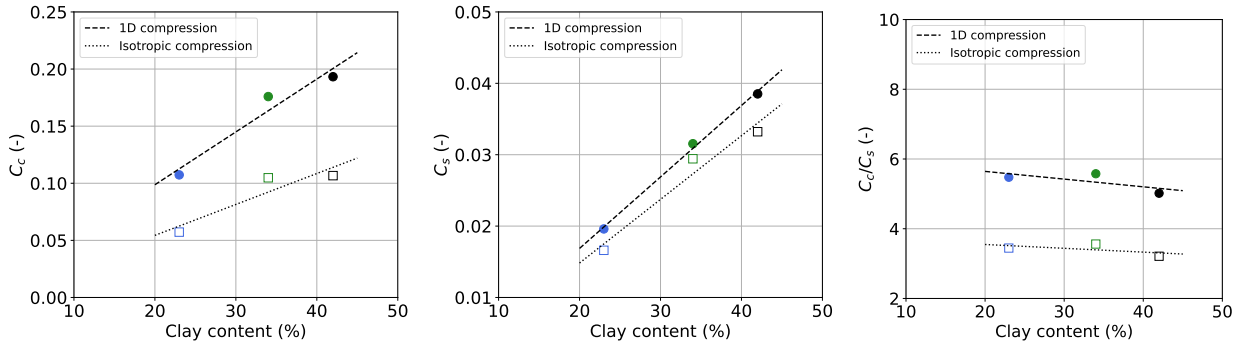

Figure 4.11: Relationship between clay content and compression properties in 1D and isotropic compression: (a) Compression index (C_c), (b) Swell index (C_s) , and (c) Ratio of compression to swell indices (C_c/C_s)

The difference in the degree of swelling observed between the triaxial and oedometer tests can be attributed to two main factors. First, the triaxial test used back pressure saturation at high pressure, gradually increasing the back pressure to dissolve air and replace it with water. In contrast, the oedometer test samples were soaked in the cell for 48 hours, relying on capillary action to draw water into the pores. Second, triaxial test samples were allowed to swell in three dimensions, while the oedometer test sample was enclosed by a ring, restricting swelling to the vertical direction. This radial constraint is significant, as confirmed by the assessment of axial and radial strains during swelling in the triaxial tests. As shown in Figure 4.12, the radial strains in the triaxial test were approximately three times larger than the axial strains, leading to a much higher degree of swelling compared to the oedometer tests. It is also important to note that the initial flat portions of the compression response in Figure 4.10 may reflect a combination of two competing mechanisms, namely swelling and compression.

Table 4.7: Isotropic and one-dimensional compression characteristics

Group	Clay Content (%)	Sample ID	C_c (-)	C_s (-)	$\sigma'_{v,comp}$ (kPa)
1	42	TX-1A	0.107	0.033	-
		OED-1	0.193	0.039	90
2	34	TX-2B	0.105	0.029	-
		OED-2	0.176	0.032	100
3	23	TX-3B	0.057	0.017	-
		OED-3	0.107	0.020	110

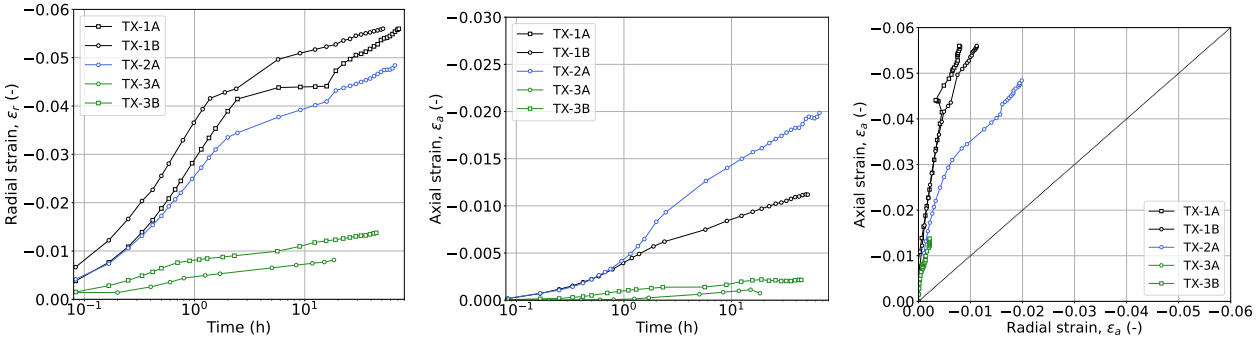

(a) (b) (c)

Figure 4.12: Radial and axial strain evolution during back pressure saturation in the triaxial tests

Correlations with Index Properties

The compressibility of silty clays increases with a higher clay content, as documented in several studies (Cola and Simonini, 2002; Nocilla et al., 2006; Anantanasakul and Roth, 2018). The literature presents various correlations between the compression coefficient and index properties for fine-grained soils. Notably Skempton (1944) for remoulded clays and Terzaghi and Peck (1967) for normally consolidated clays. The experimental data are compared with these established correlations in Figure 4.13. It is anticipated that soil compacted at the optimum water content and maximum dry density will exhibit much lower compressibility than remoulded and natural fine-grained soils.

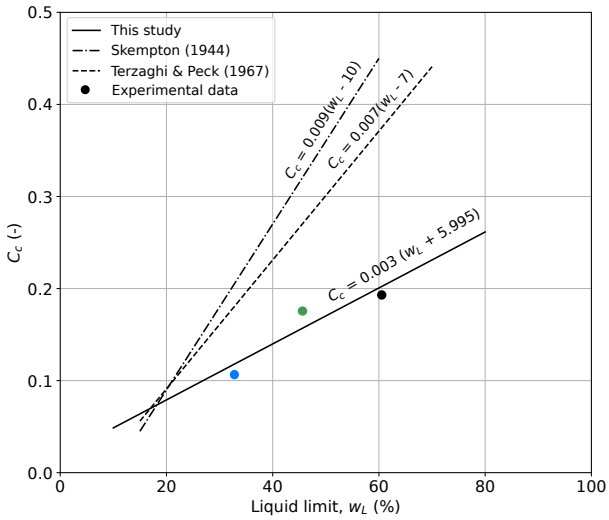

Figure 4.13: Correlation of compression coefficient (C_c) with Liquid limit (w_L)

Compaction Induced Yield Stress

During compaction, the energy supplied is absorbed by the soil skeleton as intergranular stress and by the pore fluids. Upon completion, an induced pre-stress is present in the soil, which is not necessarily equal to the compaction pressure (Dibernardo & Purdue, 1979). The compaction yield stress is critical for understanding and modelling the behaviour of compacted clay. It is analogous to the pre-consolidation pressure of natural soil, with its value being influenced by factors such as compaction conditions, the presence of coarse fractions, and the soil structure (e.g., flocculant or dispersed), which are products of clay mineralogical composition (Lambe, 1958; Prakash et al., 2014). The compaction-induced yield stress, reported in Table 4.7, was

determined from the one-dimensional compression line, using the log-log method (Sridharan et al., 1991), with values ranging from 110 kPa for material type I to 90 kPa for type III. One-dimensional compression test was extended to a higher stress level (600 kPa), making it more suitable for yield stress determination than the isotropic compression tests, which were limited to 115 kPa.

4.3.5 Shear behaviour

The following subsections describe the deviatoric stress-strain and volumetric responses from drained and undrained shearing, revealing key trends and insights into the underlying mechanisms influencing the shear behaviour.

Deviatoric Response

The deviatoric stress-strain response, illustrated in Figure 4.14, reveals a consistent strain-hardening behaviour across all the samples sheared under undrained conditions even at large strains. Only sample TX-3C sheared under stress-controlled drained conditions shows a peak deviatoric stress followed by a small reduction with the deviatoric strain. The observed strain-hardening behaviour deviates from the typical peak stress response observed in pure clays and aligns more closely with the behaviour of silt and sand (Terzaghi & Peck, 1967; Yang et al., 2001).

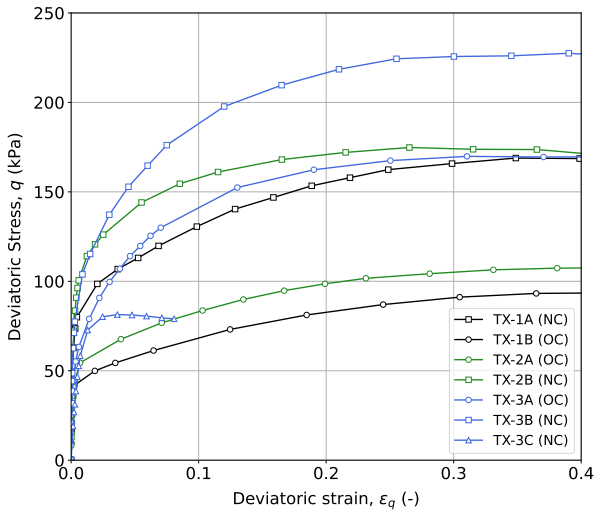

Figure 4.14: Deviatoric stress-stain response from triaxial compression tests

Volumetric Response

The evolution of excess pore pressure during undrained shearing, shown in Figure 4.15a, and the stress paths in Figure 4.15b indicate the presence of both contractive and dilative tendencies during shearing. The point of maximum excess pore pressure represents the transition from a contractive to a dilative response, marked in magenta in Figure 4.15.

In normally consolidated samples, the initial contractive phase leads to a buildup of excess pore pressure, with samples of material type I, which has the highest clay content, exhibiting the greatest increase. These findings differ from the observations discussed in Chapter 2, the results do not align with the observations made by Cola and Simonini (2002) on silty Venice lagoon soils and Anantanasakul et al. (2012) on silt-clay mixtures, which showed larger pore pressure changes in materials with decreased clay content and increased silt content during undrained shearing. Instead, they align with the general perception that

normally consolidated soils exhibit greater contractive tendencies during shear with higher clay content. The peak excess pore pressure is followed by a decay, reflecting the soil's dilative response. Samples of material type III exhibit a more pronounced decay compared to types I and II, likely due to the greater dilative tendency of more granular soils. These observations align with those made by Nocilla et al. (2006).

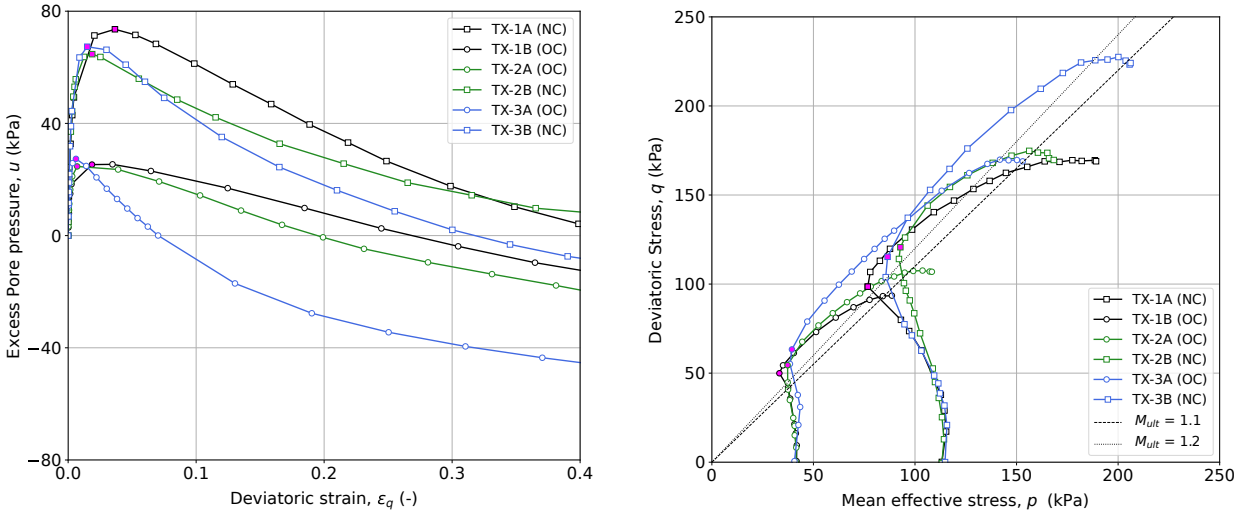

(a) (b)

Figure 4.15: Stress path (a) and excess pore pressure (b) evolution during triaxial compression tests

Sample TX-3C demonstrated immediate dilation upon drained shearing, as indicated by the negative volumetric strain shown in Figure 4.16. This response could be a reflection of the overconsolidated stress state induced due to compaction. The response could also imply that the swelling during saturation did not completely erase the stress history of the soil imparted by the compaction effort.

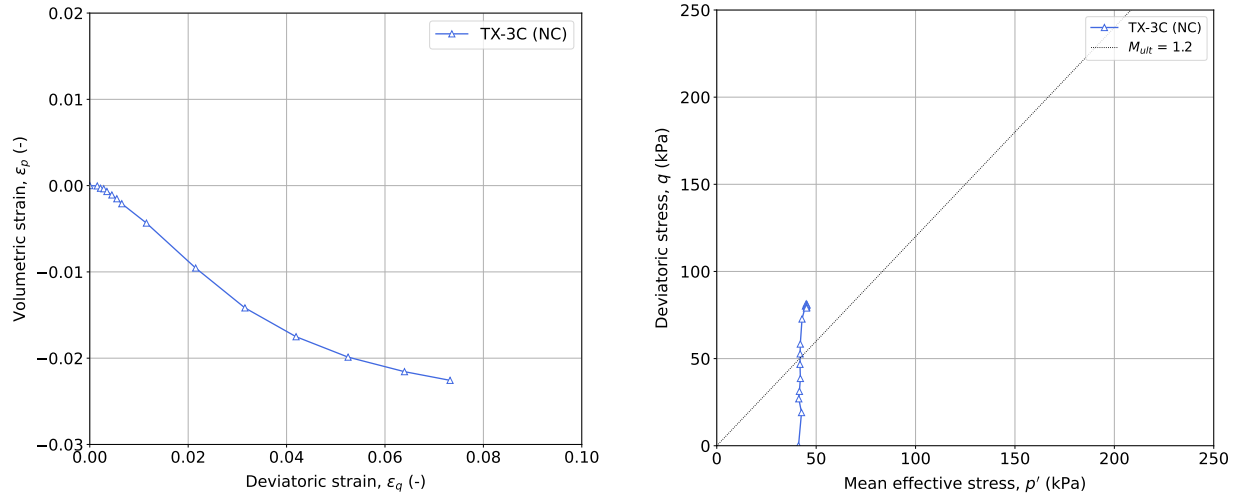

(a) (b)

Figure 4.16: Volumetric strain response (a) and stress path (b) from drained triaxial test, TX-3C

Stress Ratio

The coupled deviatoric and volumetric response of the samples upon shearing is summarised in Figure 4.17, showcasing the relationship between stress ratio, q/p', and overconsolidation ratio (OCR) and clay content. The stress ratio increases more rapidly and reaches higher peak values with increasing OCR and decreasing clay content, indicating a stiffer response. Generally, the stress ratio peaks between 1.3 and 1.7, followed by an asymptotic decrease to an ultimate value of 1.1 for material types I and II, and 1.2 for type III.

The data points corresponding to the peak and ultimate stress ratios are highlighted in red and orange, respectively, in Figure 4.17a, and are also indicated on the stress path in Figure 4.17b. The ultimate stress ratios of 1.1 and 1.2 correspond to ultimate friction angles of 27.6° and 30.0°, respectively. Figure 4.18 presents the variation of ultimate and peak friction angles for normally consolidated and overconsolidated samples of the three material types.

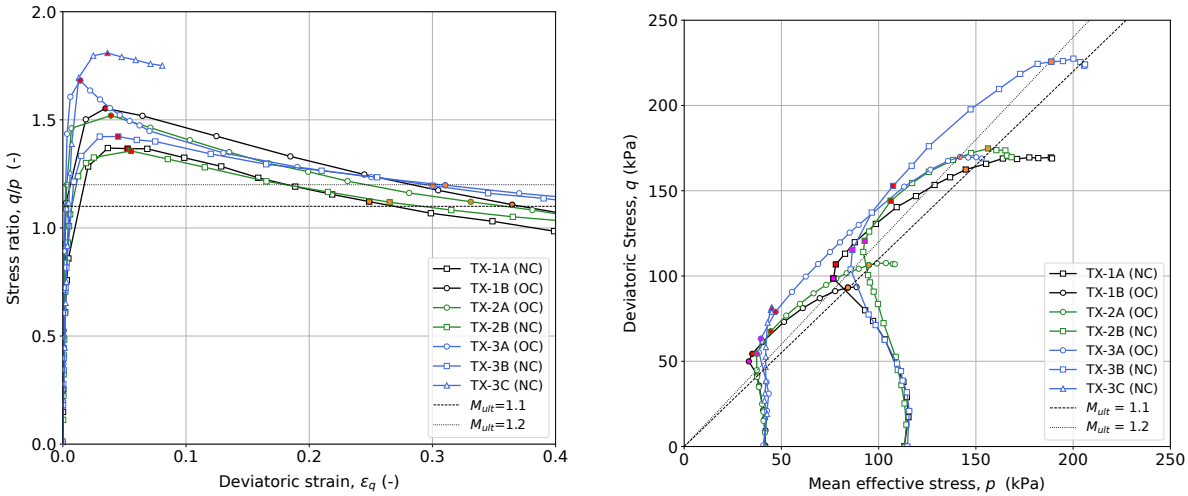

(a) (b)

Figure 4.17: Stress ratio versus deviatoric strain (a) and stress path (b) during shearing

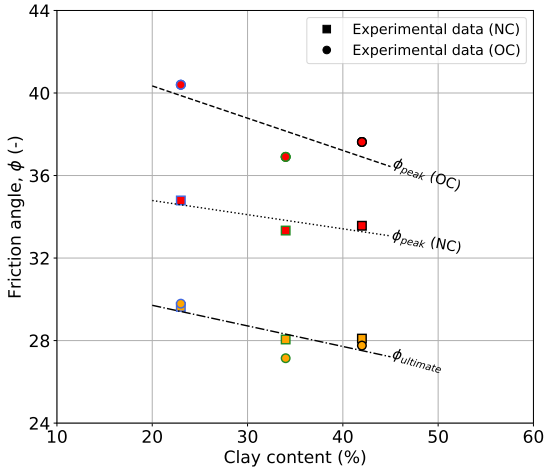

Figure 4.18: Variation of ultimate and peak friction angles with clay content

It is important to note that determining the ultimate stress ratio is subjective, as the observed stress ratio does not arrive at an asymptotic value, and continues to decrease even at strains up to 40% (Fig. 4.17a).

This is evident from the final portion of the stress path presented in Figure 4.17b, where the stress path does not asymptotically align along a constant stress ratio but instead flattens out to become horizontal. This behaviour could be attributed to sample-apparatus interaction effects (i.e., end restraint), as confirmed by the CT scans of samples T-1A and TX-1B in Figures 4.19a to 4.19f, which show the formation of "dead zones" at the top and bottom of the samples where lateral deformation is restricted.

The rough end platens used in the triaxial tests introduce a notable constraint on the samples deformation. Consequently, the unrestrained deformation, crucial for understanding the soil intrinsic behaviour, is confined to a central "free failure zone." As axial strain progresses, the two dead zones merge and form connected dead wedges which force the lateral expansion of the external portion of the sample (Muraro, 2019). The non-uniformity of boundary conditions imposed on a sample in standard triaxial testing has been experimentally studied on sands and clay by (Barden & McDermott, 1965; Duncan & Dunlop, 1968; Rowe & Barden, 1964). The size of this zone depends on the shear strength and compressibility of the soil. Consequently, measurements of pore pressure at the top and bottom of the sample, and deviatoric stress at large strain are not fully representative of the material behaviour and may introduce bias in the test interpretation.

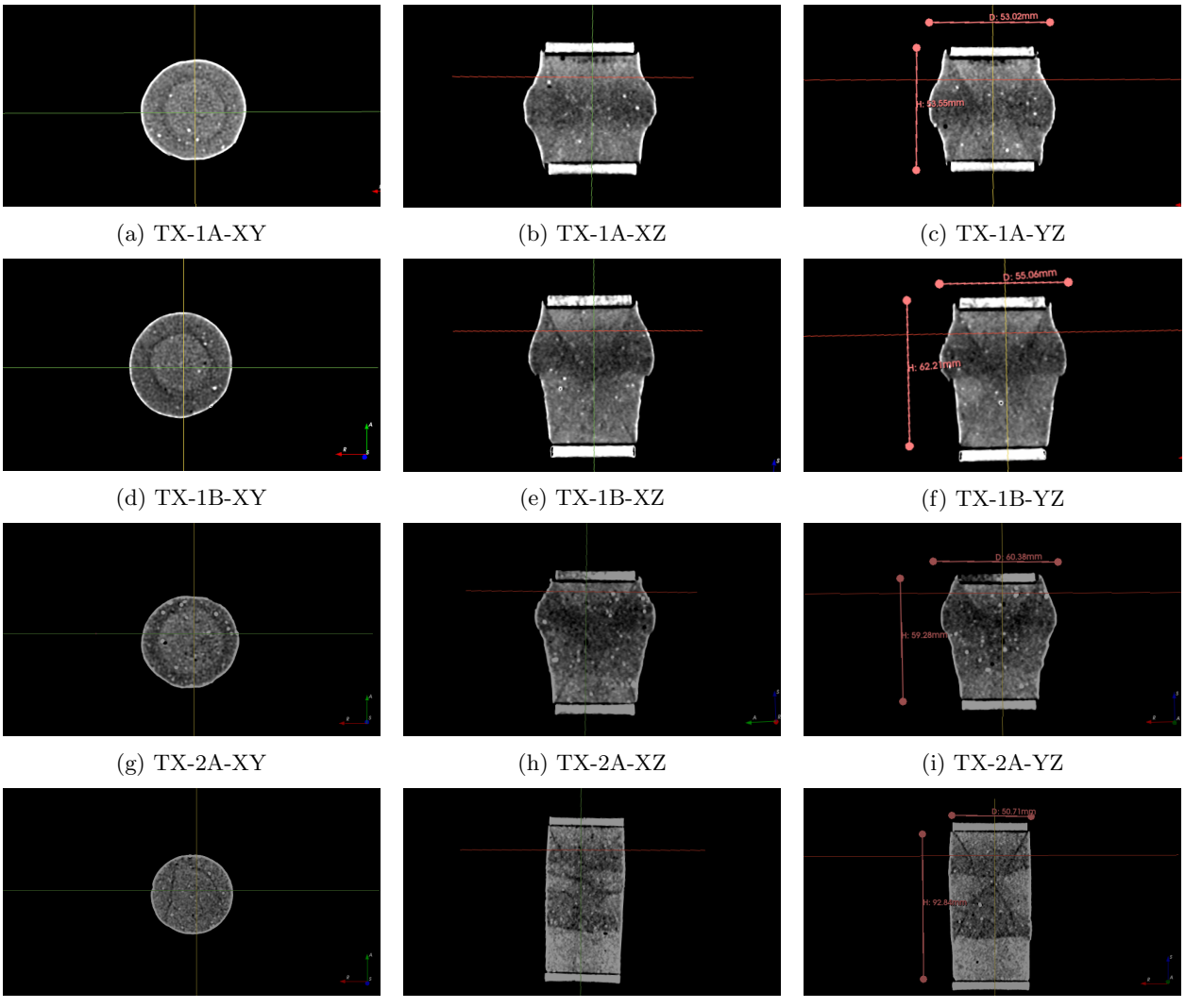

(a) TX-1A-XY (b) TX-1A-XZ (c) TX-1A-YZ

(d) TX-1B-XY (e) TX-1B-XZ (f) TX-1B-YZ

(g) TX-2A-XY (h) TX-2A-XZ (i) TX-2A-YZ

(j) TX-3C-XY (k) TX-3C-XZ (l) TX-3C-YZ

Figure 4.19: CT scans for samples TX-1A, TX-1B, TX-2A and TX-3C after testing

4.3.6 Undrained shear strength

In the context of engineering applications, the undrained shear response from the triaxial test is typically used to derive the undrained shear strength, S_u, which is often used in limit equilibrium analyses to assess dike stability. The current practices involve three different approaches to determining the undrained shear strength at the following points:

1. **Approach 1:** The point of transition from contractive to dilative behaviour, known as the phase transformation point (marked in magenta in Figure 4.15a and 4.15b).
2. **Approach 2:** The point of peak stress ratio (marked in red in Figure 4.17a and 4.17b).
3. **Approach 3:** The point at the ultimate stress ratio (marked in yellow in Figure 4.17a and 4.17b)).

Two important observations can be made from the undrained shear strength variation across the three different materials and the three different approaches:

- The undrained shear strength values determined at the phase transformation point and the peak stress ratio are more closely aligned, whereas the values derived from the ultimate stress ratio are generally much higher as a result of the large dilation exhibited by the samples.
- The variation of the undrained shear strength across the three materials with varying clay content is minimal when determined at the phase transformation point (Approach 1). This indicates that the phase transformation point could provide a more consistent approach to estimating the shear strength with varying material composition.

Due to previously discussed constraints introduced by the rough end platens in the triaxial test set-up, determining the ultimate stress ratio is subjective, as it does not reach an asymptotic value due to strain localisation. This introduces uncertainty about whether the triaxial test sample serves as a representative volume element at these strain levels. Therefore, caution must be exercised when selecting the undrained shear strength from laboratory data, and guidelines for this selection should be proposed.

Table 4.8: Undrained shear strength variation across tested samples using three approaches

	Sample ID	CC	Undrained shear strength, S_u		
			Phase transformation	Peak stress ratio	Ultimate stress ratio
		(%)	(kPa)	(kPa)	(kPa)
Normally consolidiated samples	TX-1A	42	53.4	56.5	81.0
	TX-2B	34	60.3	72.0	87.0
	TX-3B	23	57.5	76.0	112.5
Over-consolidated samples	TX-1B	42	25.0	27.0	46.5
	TX-2A	34	27.3	33.8	53.5
	TX-3A	23	31.7	39.5	85.0

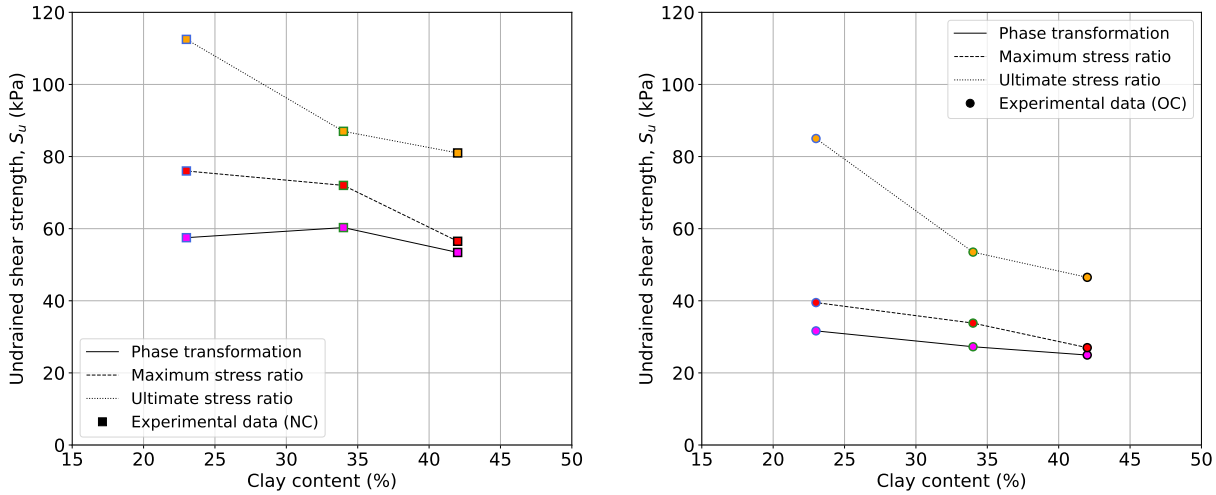

Figure 4.20: Undrained shear strength determined using three approaches (a) Normally consolidated samples (b) Overconsolidated samples

4.4 Discussion

The three tested materials, with clay content ranging from 23% to 42%, exhibited varying levels of erosion resistance. Characterization tests performed indicate that mixtures prepared with a dry mass ratio of 1:1 and 4:1, being the ratio of material type I to III, achieve the required erodibility requirements to be used in dike reinforcement, and Mix III (4:1) most closely resembled the erodibility of material type II. Microstructural analysis revealed that materials of type I and II are more similar to each other compared to material III. Materials I and II displayed a denser, more compact microstructure, contributing to higher erosion resistance. In contrast, material III showed a looser, more granular, and open structure. On the other hand, material types I and II may be more susceptible to degradation upon drying compared to III.

The mechanical testing campaign, which included oedometer and triaxial compression tests, was designed to compare material responses under similar loading and stress histories. The results revealed a clear dependency of compressibility on clay content, with higher clay percentages leading to increased compressibility. Additionally, the results indicated that the saturation method significantly influenced the compression response in triaxial tests.

The shear response of the materials was characterised by strain hardening, with samples exhibiting both clay-like (contraction) and sand-like (dilation) behaviours due to their mixed composition. Materials I (42% clay) and II (34% clay) demonstrated nearly identical responses, suggesting they would perform similarly under environmental and anthropogenic stresses. Triaxial samples effectively served as representative volume elements (RVEs) up to a certain strain level, beyond which localised deformations became prominent, as evident from post-test CT scans.

To effectively translate these laboratory findings into practical engineering applications, it is crucial to develop a constitutive model that accurately captures the observed soil behaviour under various loading conditions. Such a model would provide a reliable tool for predicting the performance and stability of geotechnical structures.

Chapter 5

Constitutive Modelling

This chapter assesses the capability of the newly developed JMC-clay Bounding Surface model for Dutch clays, as introduced by Chao (2024), using the new experimental data presented in Chapter 4. The chapter begins with a discussion of the model background and formulation, followed by a detailed modelling approach that includes calibration and initialisation. The model is then validated through a comparative analysis of its predictions of the compression and shear response against experimental data.

5.1 Background Information

The JMC-clay bounding surface model extends the JMC clay elastoplastic model formulation, to incorporate bounding surface plasticity. This approach allows for plastic deformation within the bounding surface, with the rate depending on the proximity between the current stress point and its "image" on the bounding surface (Dafalias, 1981). This was motivated by the soil behaviour, even within the yield locus, being rarely ever elastic. Other features of the JMC-clay BS include:

- Bounding surface shape flexibility
- Non-associated plasticity
- Hybrid flow rule
- Mixed volumetric and distortional hardening
- Rotational hardening

5.2 Model Formulation

This section summarises the formulation of the JMC- clay BS as outlined in Chao (2024), including the bounding surface, the plastic potential and the hardening law.

The JMC bounding surface expression presented in Equation 5.1 is reformulated from JMC-clay elastoplastic yield locus, which was originally an extension of the expression proposed by Mcdowell and Hau (2003) to account for anisotropy. The proposed bounding surface allows flexibility in the shape through the two coefficients k_f and M_f.

$$F = \left(\bar{q} - \bar{p'}\alpha_f\right)^2 + \frac{M_f^2 - \alpha_f^2}{k_f - 1}\bar{p'}^2 - \frac{M_f^2 - \alpha_f^2}{k_f - 1}{p'_0}^2 \left(\frac{\bar{p'}}{p'_0}\right)^{\frac{2}{k_f}} \tag{5.1}$$

Where,

$\bar{p'}$: Image mean effective stress on the bounding surface
$\bar{q}$: Image deviatoric stress on the bounding surface
α_f : Inclination of the bounding surface in p'-q space
M_f, k_f : Shape coefficients of the bounding surface
p'_0 : Size of the bounding surface

The image stress on the bounding surface is related to the current stress state through the radial mapping rule as proposed by Seidalinov (2018).

$$\bar{p'} = p'_c + b \cdot (p' - p'_c); \bar{q} = q'_c + b \cdot (q - q'_c) \tag{5.2}$$

b : Similarity ratio
p'_c, q_c : Projection centre

The plastic potential, presented in Equation 5.5 involves a non-dimensional anisotropic variable, α_g. By defining the inclination of the plastic potential, it accounts for the deviatoric and volumetric plastic strain rates coupling and introduces the anisotropic response in the plastic deformation mechanism.

$$G = \left(\bar{q} - \bar{p'}\alpha_g\right)^2 + \left(M_g^2 - \alpha_g^2\right)\bar{p'}(\bar{p'} - p'_g) \tag{5.3}$$

Where,

α_g : Parameter defining inclination of the plastic potential
M_g : Critical state stress ratio
p_g : Dummy variable to determine the size of the plastic potential

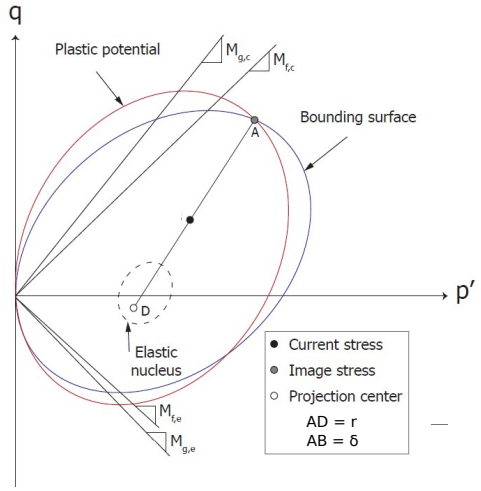

Figure 5.1: Sketch of elastoplastic bounding surface concept

The plastic modulus K_p for any stress state (p, q) is related to a bounding plastic modulus $\bar{K_p}$ at the corresponding image stress $(\bar{p'}, \bar{q})$ using the Euclidean distances, δ, between image stress and current stress state, and r, between image stress and projection centre (Fig. 5.1), as denoted in Equations 5.4 to 5.6.

$$\frac{r}{\delta} = \frac{b}{(b-1)} \tag{5.4}$$

$$K_p = \bar{K_p} + \frac{h{p'_0}^3\delta}{\langle r - s\delta \rangle} = \bar{K_p} + \frac{hp'_0}{\langle \frac{b}{b-1} - s_{\text{eln}} \rangle}\left(\frac{p'_0}{p'_{\text{ref}}}\right)^2 \tag{5.5}$$

$$\bar{K_p} = -\left(\frac{\partial F}{\partial p'_0}p'_0 + \frac{\partial F}{\partial \alpha}\alpha\right) \tag{5.6}$$

Where,

h : Positive shape hardening variable
s_{eln} : Parameter controlling the relative size of the elastic nucleus
p_{ref} : Reference pressure ensuring unit consistency

When $s_{\mathrm{eln}} = 1$, the elastic nucleus is reduced to a single point located at the projection centre. Additionally, the plastic modulus, K_p, is defined in line with the consistency condition of the bounding surface, expressed as $\dot{F} = 0$.

The shape hardening variable h can evolve with an internal variable d to reproduce cyclic degradation or shakedown, caused by the accumulation of plastic deviatoric strain, to accurately model the continuous evolution of the stress-strain curve upon cyclic loading as observed in the laboratory. This model adopts the formulation by Shi et al. (2018) presented in Equations 5.7 and 5.8, where h_0 and a_d are model parameters.

$$h = \frac{h_0}{1+d} \tag{5.7}$$

$$\delta d = \begin{cases} a_d(1+d)|\delta\varepsilon_q^p|, & \text{if } a_d < 0 \\ a_d|\delta\varepsilon_q^p|, & \text{if } a_d \geq 0 \end{cases} \tag{5.8}$$

A hybrid flow rule is presented in Equation 5.9 is implemented in the model, as proposed by Shi et al. (2018), in which the volumetric plastic strain increment is not solely dependent on the image stress state. Instead, it is contributed by both current stress and image stress, as defined in 5.10 through x. While the deviatoric plastic increment is only contributed by the image stress.

$$\frac{\partial G_{\mathrm{hyb}}}{\partial p'_{\mathrm{hyb}}} = \frac{\partial G_{\mathrm{img}}}{\partial \bar{p'}} \cdot x + \frac{\partial G_{\mathrm{cur}}}{\partial p'} \cdot (1-x) \tag{5.9}$$

$$x = (1/b)^w \tag{5.10}$$

$$\frac{\partial G_{\mathrm{hyb}}}{\partial q_{\mathrm{hyb}}} = \frac{\partial G_{\mathrm{img}}}{\partial \bar{q}} \tag{5.11}$$

b : similarity ratio
w : Model parameter

Subscripts *img* and *cur* denote the plastic potential defined at the image and current stress state. The image stress flow rule is regained when $w = 0$.

Two hardening laws are included in the formulation of the model to control the size and inclination of the bounding surface. Through mixed distortional and volumetric hardening, the first hardening rule governs the evolution of the size of the bounding surface, ruled by volumetric and deviatoric strains as given by Equations 5.12 and 5.13. This was originally proposed for granular soils (Nova, 1977; Nova & Wood, 1979) and recently also for fibrous organic soils such as peat (Muraro & Jommi, 2021).

$$\frac{\delta p'_0}{p'_0} = \frac{v}{\lambda - \kappa}\left(\delta\varepsilon_{\mathrm{p}}^{\mathrm{p}} + D\delta\varepsilon_{\mathrm{q}}^{\mathrm{p}}\right) \tag{5.12}$$

$$D = D_0 \exp\left(-D_1\varepsilon_q^p\right) \tag{5.13}$$

Where,

ν : Specific volume of the soil
λ : Slope of the isotropic normal compression line
κ : Slope of the isotropic unloading-reloading line
$\delta\varepsilon_{\mathrm{q}}^{\mathrm{p}}$: Deviatoric plastic strain increment
$\delta\varepsilon_{\mathrm{p}}^{\mathrm{p}}$: Volumetric plastic strain increment
D_0, D_1 : Deviatoric strain hardening parameters

A second hardening rule governs the rotation of the bounding surface produced by plastic straining. The rotation rule derived for the plastic potential (Equation 5.3) is also used for the bounding surface. The rotation rate, $\delta\alpha = \delta\alpha_g = \delta\alpha_f$, given in Equation 5.14, was adopted from Dafalias and Taiebat (2013).

$$\delta\alpha = \langle L \rangle c p_{\mathrm{atm}} \frac{p'}{p'_0} (\alpha_b - \alpha) \tag{5.14}$$

Where,

L : Plastic multiplier, enclosed in Macauley brackets $\langle\rangle$ to track plastic loading and elastic unloading
p_{atm} : Atmospheric pressure
p'_0 : Size of the bounding surface
c : Parameter controlling the rate of rotation

In developing this model, the post-yielding plastic deformation response from experimental data was analysed in terms of the inclination of the plastic strain increment vectors along stress paths at constant stress ratios. The analysis revealed a progressive reorientation of these vectors towards radial paths, eventually reaching a fairly constant inclination after sufficient straining. To capture this behaviour, the model incorporated an asymptotic bounding value, α_{gb}, for different radial paths, calculated by modifying the original expression proposed by Dafalias and Taiebat (2013) and presented in Equation 5.15 for triaxial compression ($\eta \geq 0$) and extension ($\eta < 0$).

$$\alpha_{gb} = \begin{cases} \frac{M_{g,c}}{z_c} \left[1 - \exp\left(-s \frac{|\eta|}{M_{g,c}}\right)\right]^y & \text{if } \eta \geq 0 \\ -\frac{M_{g,e}}{z_e} \left[1 - \exp\left(-s \frac{|\eta|}{M_{g,e}}\right)\right]^y & \text{if } \eta < 0 \end{cases} \tag{5.15}$$

where z_e, z_c, y, and s are positive model constants.

The described model formulation was implemented by Chao (2024) using a computational driver employing a single Gauss point scheme. This approach facilitates the simulation of various loading conditions, ensuring accurate numerical integration and efficient computation of the stress-strain response.

5.3 Modelling Approach

5.3.1 Calibration Approach

As mentioned in the methodology in Chapter 2, data from tests on material types I and III will be used to calibrate the model. A step-by-step calibration approach was adopted to emphasise the influence of specific constitutive ingredients on the model prediction, through direct comparison with laboratory data. Three calibration attempts were made to highlight the differences between isotropic and anisotropic model formulations, and the shape effect of the bounding surface. The model features activated in each calibration attempt are outlined in Table 5.1.

Table 5.1: Ingredients of the JMC-clay BS Model used in the calibration attempts

Feature	Attempt 1	Attempt 2	Attempt 3
Bounding surface	✓	✓	✓
Volumetric hardening	✓	✓	✓
Distortional hardening	✓	✓	✓
Rotational hardening (anisotropy)			✓
MCC bounding surface shape - k_f=2.0	✓		✓
Bounding surface shape - k_f=1.25		✓	
Non-associated flow rule		✓	

5.3.2 Model Parameters

The model requires the calibration of 18 parameters as follows:

- λ, κ: determined from the one-dimensional compression curve obtained from oedometer tests
- ν: assumed equal to 0.3
- $M_{g,c}$: determined from triaxial compression tests
- $M_{g,e}$: assumed $0.8M_{g,c}$; however, this does not affect the numerical predictions reported in this study, as all experimental tests were conducted along compressive axisymmetric stress paths
- z_c, z_e, s, y, c: rotational hardening coefficients usually defined from at least three triaxial tests (a K_0 compression test and two radial paths). In this study, these parameters were derived from the laboratory tests conducted by Chao (2024) on Dutch silty clay.
- D_0, D_1: calibrated with reference to the shearing response from triaxial compression tests
- $M_{f,c}$: assumed equal to $M_{g,c}$
- k_f: determined from yielding points
- h_0: calibrated with reference to isotropic triaxial compression
- s_{eln}, a_d, w : calibrated with reference to cyclic triaxial tests

5.3.3 State Variables

Five initial state variables are needed for the initialisation of the adopted model:

- e_i: initial void ratio
- (p'_{0i}, q_i): initial stress state at the beginning of the test
- $p'_{b0,i}$: initial size of the bounding surface
- α_i: initial inclination of the bounding surface and plastic potential
- (p'_c, q_c): initial location of the projection centre

The initial inclination of the bounding surface was determined using the equation 5.16 described by Dafalias et al. (2006), assuming K_0^{NC} using Jaky's simplified relationship.

$$\alpha_{\mathrm{i}} = \frac{\mathrm{B}\varepsilon\eta_{\mathrm{K_0}}^3 + \eta_{\mathrm{K_0}}^2 + \left[2\left(1-\kappa^*/\lambda^*\right) - BM_{\mathrm{g,c}}^2\right]\varepsilon\eta_{\mathrm{K_0}} - \mathrm{M}_{\mathrm{g,c}}^2}{2\varepsilon\left(1-\kappa^*/\lambda^*\right)}$$
$$\mathrm{B} = -\frac{2(1+v)}{9(1-2v)}\frac{\kappa^*}{\lambda^*} \tag{5.16}$$

where $\epsilon = 3/2$ and η_{K0} is the stress ratio corresponding to K_0^{NC}. For normally consolidated conditions, the initial size of the bounding surface, $p'_{b0,i}$, can be computed using Equation 5.1, with α_i, and $\bar{p'}$ and $\bar{q}$ derived from the compaction-induced yield stress, $\sigma'_{v,comp}$, as determined from the 1D compression response (Section 4.3, Table 4.7) using Equations 5.17 and 5.18.

$$\bar{p'} = \frac{\sigma'_{v,comp}\left(1+2K_0^{NC}\right)}{3} \tag{5.17}$$

$$\bar{q} = \sigma'_{v,comp}\left(1-K_0^{NC}\right) \tag{5.18}$$

5.4 Model Calibration

5.4.1 Model parameters

The adopted model parameters in the three calibrations are presented in Table 5.2. Given the fact that the experimental study did not include cyclic triaxial tests, no elastic nucleus was adopted (s_{eln}=1), and parameters defining the cyclic response (a_d, w) were set to 0.

Table 5.2: Model parameters adopted in the calibration attempts

	Type	CF	λ	κ	$M_{g,c}$	$M_{g,e}$	ν	c	z_c	z_e	s	y	$M_{f,c}$	k_f	D_0	D_1	h_0
Attempt 1	I	42%	0.084	0.017	1.10	0.88	0.3	0	0	0	0	0	1.10	2.00	0.45	15	150
	III	23%	0.047	0.009	1.20	0.96	0.3	0	0	0	0	0	1.20	2.00	0.55	20	150
Attempt 2	I	42%	0.084	0.017	1.10	0.88	0.3	0	0	0	0	0	1.10	1.25	0.35	15	150
	III	23%	0.047	0.009	1.20	0.96	0.3	0	0	0	0	0	1.20	1.25	0.50	20	150
Attempt 3	I	42%	0.084	0.017	1.10	0.88	0.3	90	1.6	1.2	2.2	2	1.10	2.00	0.40	25	150
	III	23%	0.047	0.009	1.20	0.96	0.3	80	1.6	1.2	2.2	2	1.20	2.00	0.45	30	150

5.4.2 Stress-state Initialisation

Figure 5.3 presents the initial shape, size, and inclination of the bounding surface derived for each of the three calibration attempts and material types, determined using Equations 5.16 to 5.18. The yield points from one-dimensional compression tests, used to compute α_i (Section 5.3.3), are also plotted.

To aid in determining a representative initial bounding surface, estimated yield points from isotropic compression of samples TX-1A and TX-3B, are plotted on Figure 5.3. The yield points during isotropic compression were estimated from the volumetric strain versus mean effective stress plots (Figures 5.2a and 5.2c), following the approach of Wood (2014b), and are defined as the points of marked stiffness change. Additionally, the cumulative work input, W, against the stress path length, S, computed using Equations 5.19 and 5.20, was investigated to further support the yielding point estimation (Figures 5.2b and 5.2d).

$$W = \int p'\delta\varepsilon_p + q\delta\varepsilon_q \tag{5.19}$$

$$S = \sum \sqrt{\delta p'^2 + \delta q^2} \tag{5.20}$$

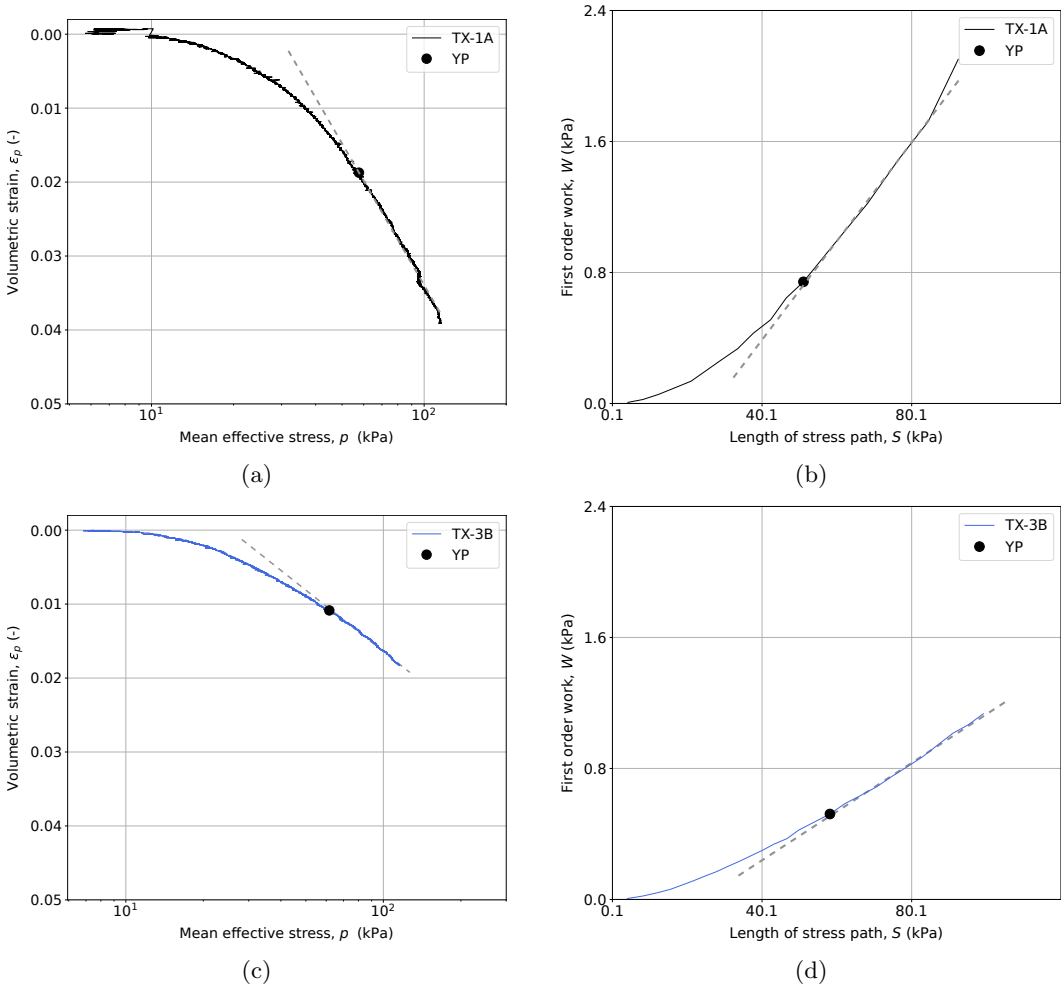

Figure 5.2: Yield point estimation from isotropic compression on sample TX-1A and TX-3B

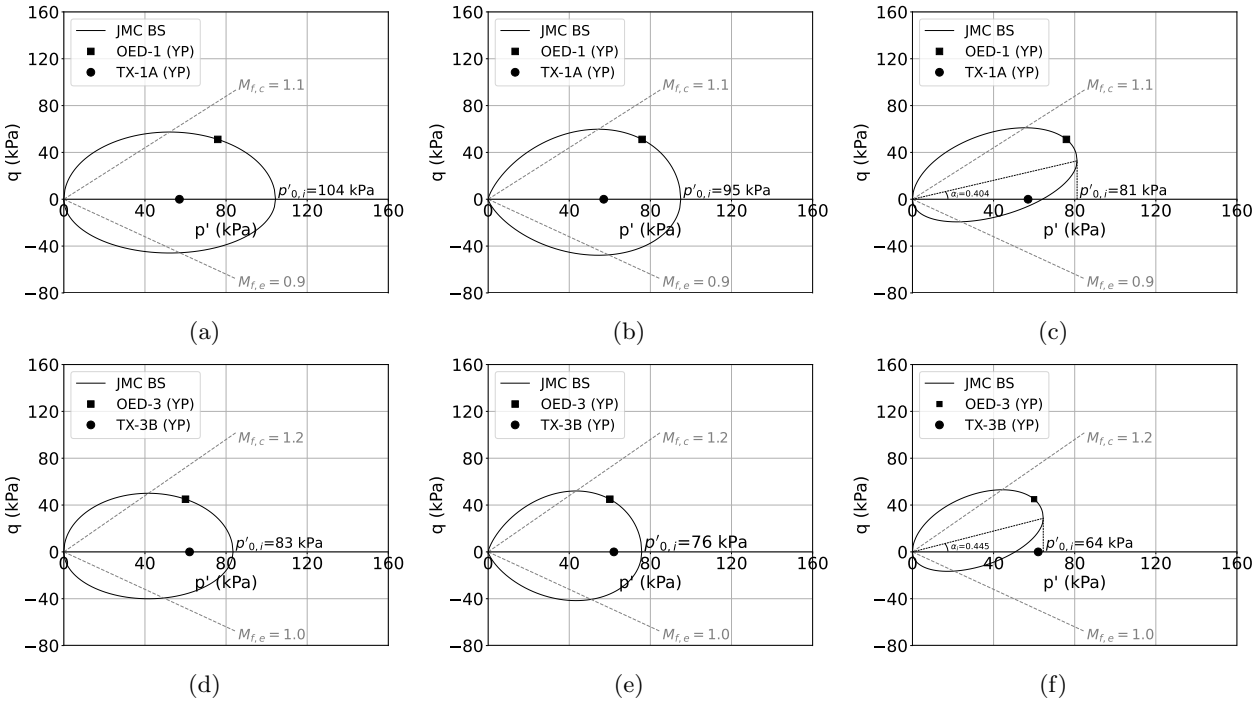

Figure 5.3: Initial bounding surface for material type I (a) Attempt 1 (b) Attempt 2 (c) Attempt 3 and material type III (d) Attempt 1 (e) Attempt 2 (f) Attempt 3

5.4.3 Calibration Results

The three calibration attempts are evaluated by comparing their predictions against experimental data, aiming to identify the parameter set that best captures the compression and shear response.

Compression Response

One-dimensional compression tests were simulated, and the results from the three attempts are presented in Figure 5.4 against the experimental data. As discussed in Section 4.3.4, the initial compression response may involve competing mechanisms of swelling and compression. Since the model does not account for residual swelling, the simulations were initialised from a higher stress state than the laboratory tests; however, this was not necessary for the isotropic compression simulations as they began from an already higher vertical effective stress imposed during the saturation ramp. Overall, the model accurately predicts the loading path for material types I and III in all attempts. However, during unloading, the model captures the general trend but does not precisely match the experimental response, particularly for material type I, predicting a stiffer response.

Figure 5.5 illustrates the isotropic compression response from the simulations of the triaxial tests. The model does not accurately capture the initial re-compression phase, underestimating the compressibility upon reloading. Nonetheless, it well predicts the void ratio at the end of isotropic compression in the three calibration attempts, more accurately for samples of material type I compared to type III.

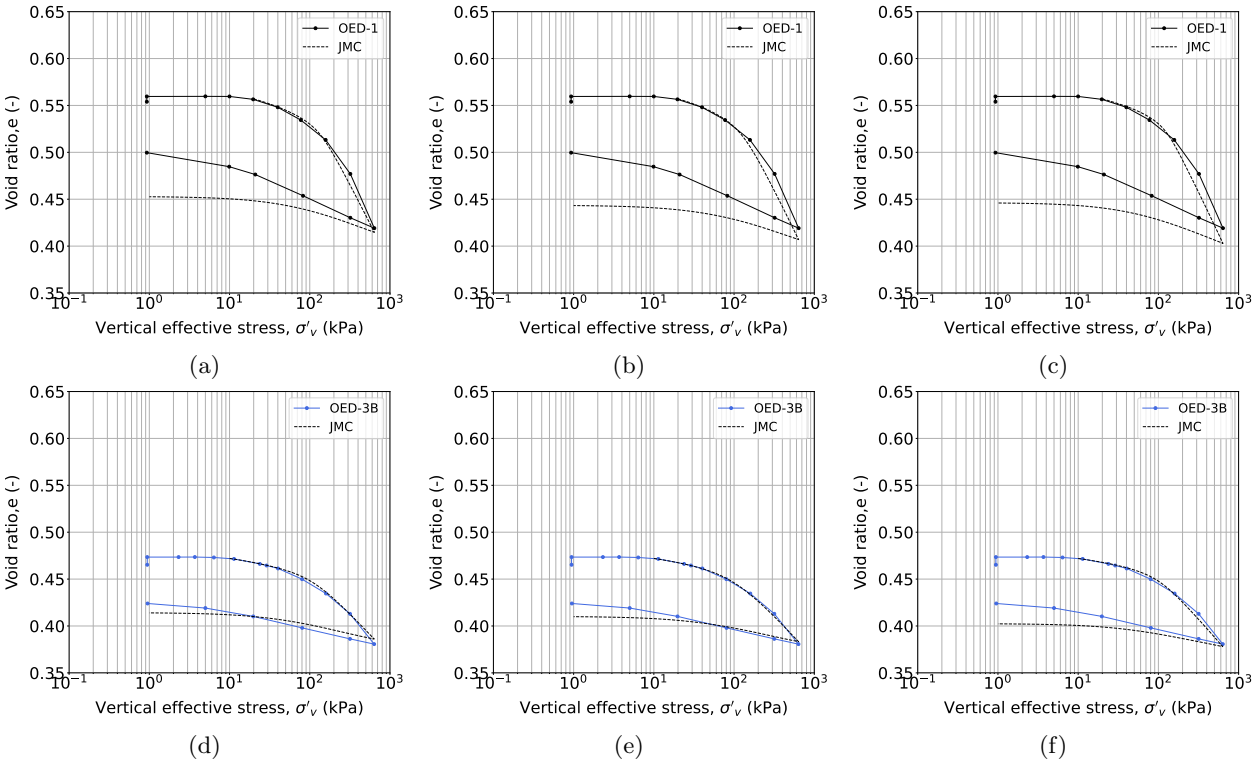

Figure 5.4: Comparison between experimental data and numerical results of 3 calibration attempts for material types I and III: One-dimensional compression response (a)(d) Attempt 1 (b)(e) Attempt 2 (c)(f) Attempt 3

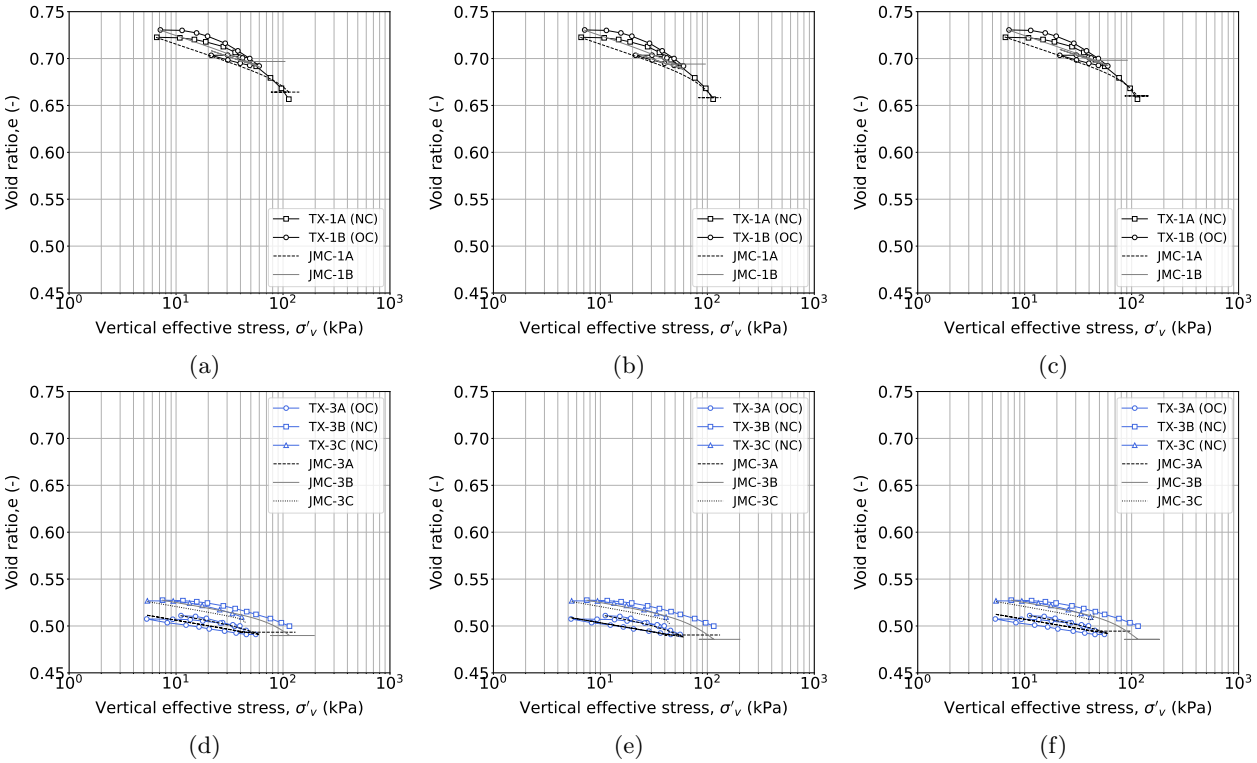

Figure 5.5: Comparison between experimental data and numerical results of 3 calibration attempts for material types I and III: Isotropic compression response (a)(d) Attempt 1 (b)(e) Attempt 2 (c)(f) Attempt 3

Shear Response

Figures 5.6 to 5.9 show the comparison between the experimental data and the numerical simulations of the undrained and drained triaxial compression tests on samples sheared from a normally consolidated and overconsolidated stress state of material type I and III, from the three calibration attempts.

The stress-strain results from the simulations, presented in Figure 5.6, demonstrate that the model generally captures the strain-hardening behaviour of the samples, but it tends to underestimate the initial stiffness across all three calibration attempts, particularly for the samples in the overconsolidated state.

In Attempts 1 and 2, which utilise an isotropic formulation, the model accurately predicts the ultimate stress for all samples but encounters challenges in capturing the overall stiffness evolution of the samples sheared from an overconsolidated state. Attempt 3, employing an anisotropic formulation, also underestimates stiffness, particularly at strains above 5.0%, but it generally predicts the ultimate stress well, except for the overconsolidated material type III (TX-3A) sample. The model accuracy at strain levels between 1% and 5% is particularly important, as these ranges are typically encountered in field applications such as dikes.

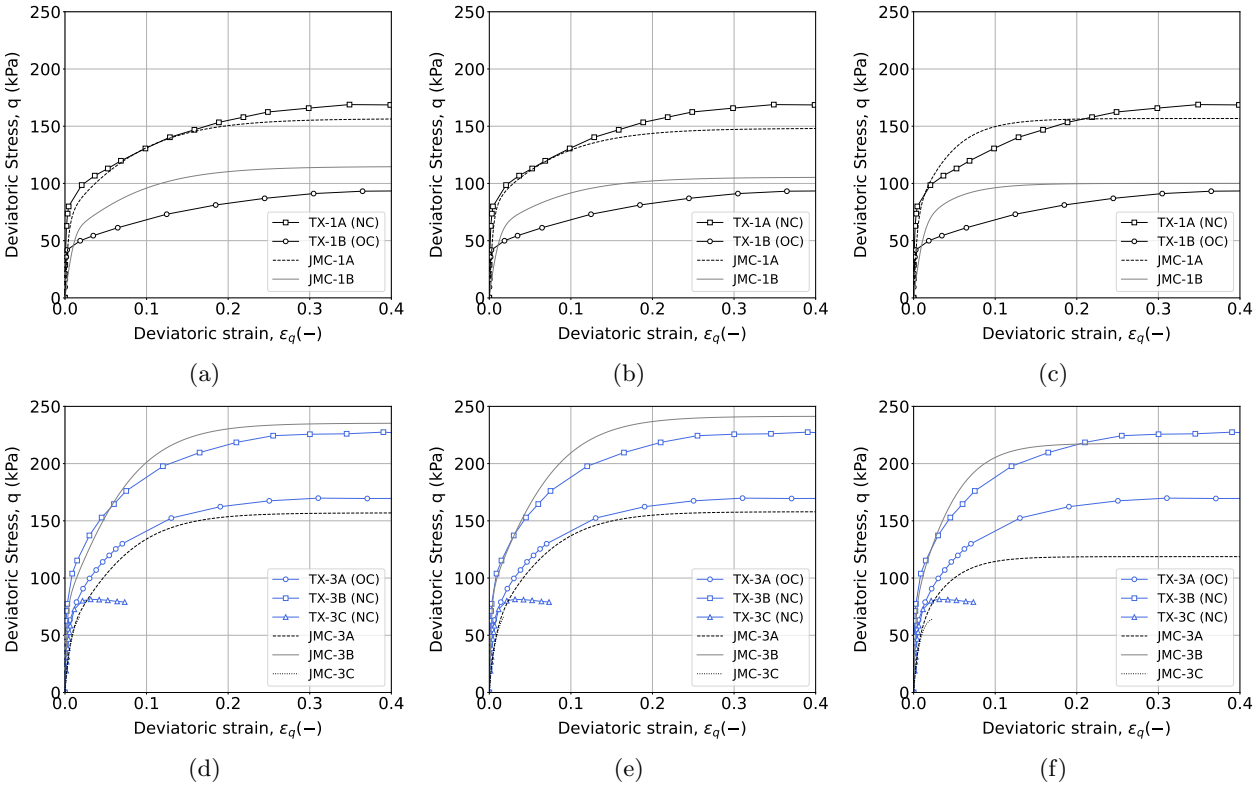

Figure 5.6: Comparison between experimental data and numerical results of 3 calibration attempts for material types I and III: Stress-strain response (a)(d) Attempt 1 (b)(e) Attempt 2 (c)(f) Attempt 3

The stress path prediction presented in 5.7 demonstrates the model's ability to capture the initial contraction and dilation due to the inclusion of distortional hardening. This feature allows the model to simulate the dilatant response after the attainment of $M_{g,c}$. The isotropic formulation with a k_f=2.00 in attempt 1 does not capture the initial contraction of samples TX-1B and TX-3A when sheared from a normally consolidated state as accurately as the isotropic formulation with a k_f=1.25 (i.e., non-associated) in attempt 2 or the anisotropic formulation in attempt 3. Both attempts 2 and 3 accurately capture the stress path, with attempt 2 excelling in predicting the stress path of samples TX-1B and TX-3A sheared from an overconsolidated state.

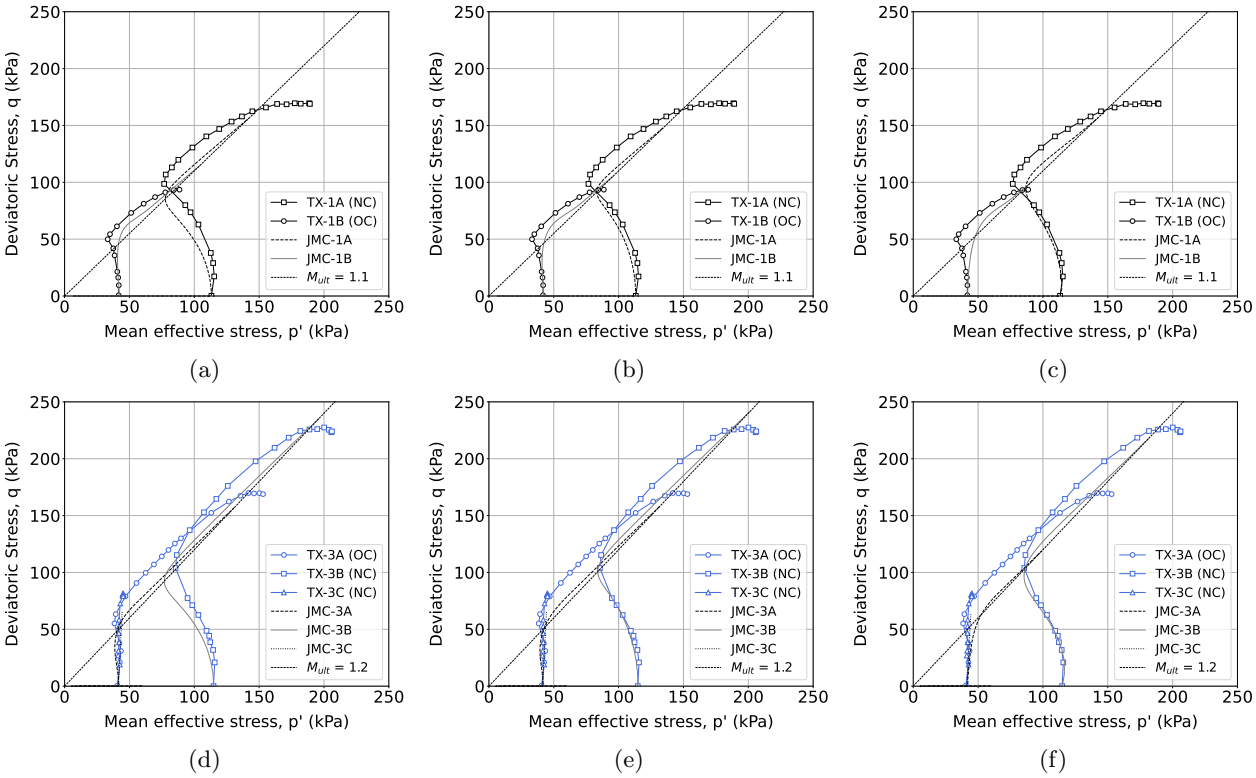

Figure 5.7: Comparison between experimental data and numerical results of 3 calibration attempts for material types I and III: Stress path (a)(d) Attempt 1 (b)(e) Attempt 2 (c)(f) Attempt 3

The predicted pore pressure response during undrained shearing (Figure 5.8) aligns with the observed stress path, with the model capturing the general trend of initial positive pore pressure (contraction) followed by decay (dilation). The model accurately predicts the peak excess pore pressure, particularly well for material type III, but tends to overestimate the final excess pore pressure due to the rapid decay, particularly in attempt 3 with the anisotropic formulation.

Figure 5.9 presents the predicted volumetric strains in the drained shearing simulation of sample TX-3C. The instant dilation observed during drained shearing of TX-3C was not captured by the isotropic formulations in attempts 1 and 2, which instead show initial contraction followed by dilation. However, the anisotropic formulation in attempt 3 successfully captured this response. The model predictions ended at an earlier deviatoric strain compared to the laboratory tests as a result of the controlled stress path imposed in the numerical simulation. On the contrary, the redistribution of stresses in the experiential test allowed the attainment of higher strain levels during the progressive loss of controllability of the test.

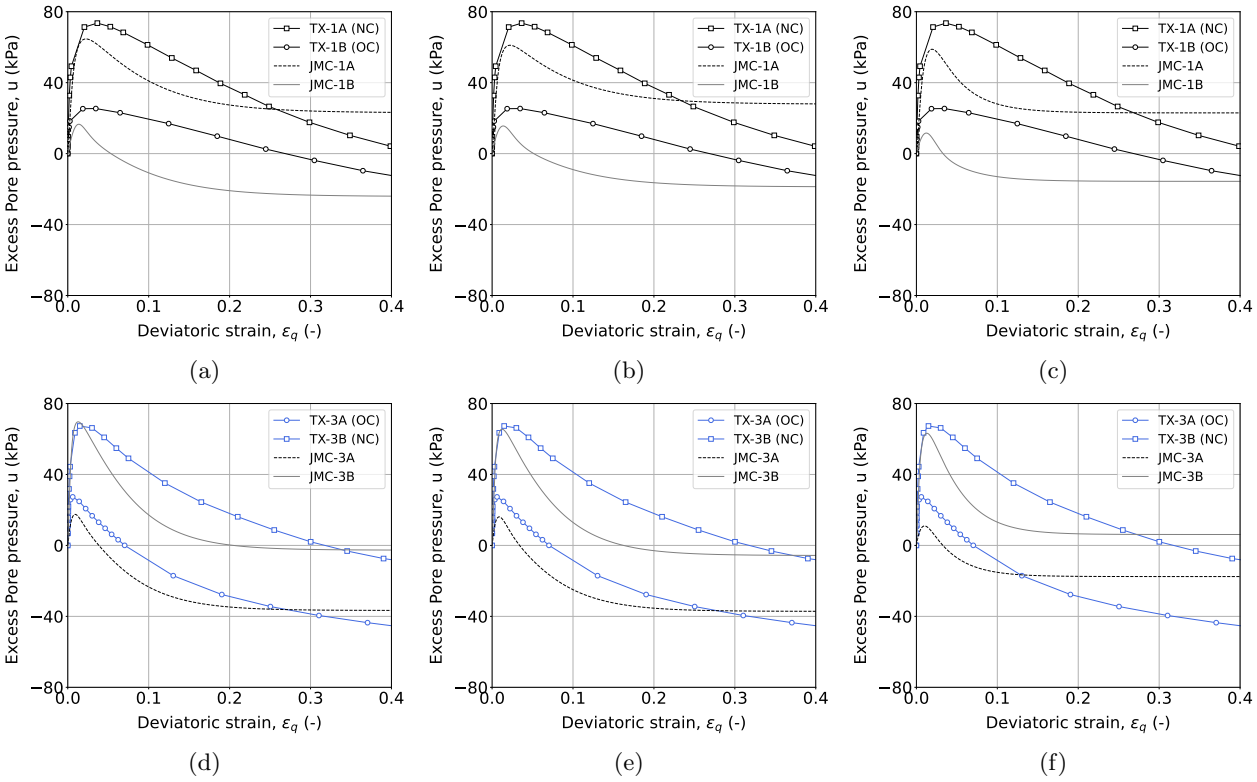

Figure 5.8: Comparison between experimental data and numerical results of 3 calibration attempts for material types I and III: Pore pressure response (a)(d) Attempt 1 (b)(e) Attempt 2 (c)(f) Attempt 3

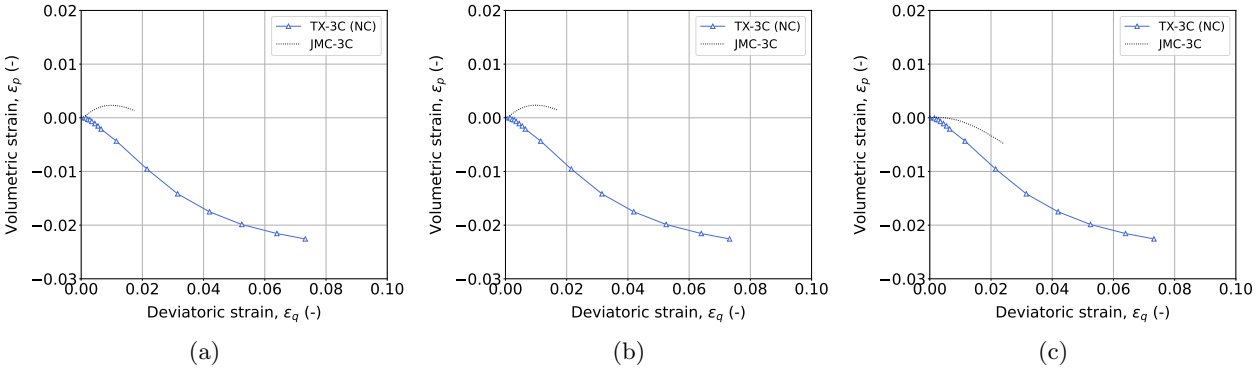

Figure 5.9: Comparison between drained triaxial compression experimental data and numerical results of 3 calibration attempts for material type III : Volumetric strain (a) Attempt 1 (b) Attempt 2 (c) Attempt 3

Calibration Conclusions

Following the systematic evaluation of the three calibration attempts, the following key observations were made:

- All three calibration attempts captured the compression response with similar accuracy.
- The stress-strain behaviour was well predicted in the three attempts. However, the isotropic formulations in Attempts 1 and 2 provided a better fit, particularly for the samples in the overconsolidated

state, compared to Attempt 3.

- The isotropic formulation with k_f=1.25 (attempt 2) and the anisotropic formulation (attempt 3) were successful in better capturing the initial contraction, as demonstrated by the comparison of the stress paths.
- The pore pressure response was predicted well across all three attempts, though a more rapid decay was predicted in Attempt 3.
- Only Attempt 3 was able to accurately capture the immediate dilation observed during the drained triaxial compression test.
- Evaluation of the yielding points from isotropic compression, as shown in Figure 5.3, indicated the points are most consistent with the inclined initial bounding surface as determined by the anisotropic formulation in Attempt 3.

Based on these observations, most of the behaviour exhibited by the samples can be captured using the isotropic model in attempt 2 with a modified shape (k_f=1.25). However, accounting for the last two points stated above, the parameter set from the final calibration attempt using the anisotropic model was adopted. It is important to note that the accurate initialisation of the stress state would typically require more tests with radial probe stress path. The following section will validate the calibrated model using experimental data from tests conducted on Material Type II.

5.5 Model Validation

To validate the predictive capabilities of the JMC-clay BS model, the calibrated parameters for material types I and III were interpolated based on clay content to estimate the parameters for material type II, as shown in Table 5.3. The bounding surface was initialised in the same manner. The accuracy of these interpolated parameters was then assessed by simulating oedometer and triaxial tests on material type II and comparing the simulation results to the corresponding experimental data, as illustrated in Figure 5.10.

Table 5.3: Predicted model parameters for material type II using material type I and III calibrated model parameters

Type	CF	λ	κ	$M_{g,c}$	$M_{g,e}$	ν	c	z_c	z_e	s	y	$M_{f,c}$	k_f	D_0	D_1	h_0
I	42%	0.084	0.017	1.10	0.88	0.3	90	1.6	1.2	2.2	2	1.10	2.00	0.40	25	150
III	23%	0.047	0.009	1.20	0.96	0.3	80	1.6	1.2	2.2	2	1.20	2.00	0.45	30	150
II	34%	0.068	0.01	1.14	0.91	0.3	86	1.6	1.2	2.2	2	1.14	2.00	0.42	27	150

The results presented in Figure 5.10 demonstrate that the model parameters can be effectively extended to encompass a range of materials by utilising the clay content as reference parameters. The model accurately predicted both the compression response (evident in Figures 5.10b and 5.10a) and the shear behaviour, encompassing both deviatoric and volumetric responses. However, the model fell short in capturing the initial contractive response, as observed in the stress path in Figure 5.10d. It is worth noting that the contractive response of the TX-2B sample did not fall neatly between the responses of material types I and III under the same stress path, contrary to what would be expected based on its intermediate clay content.

To further assess the model for engineering applications, the undrained shear strength was determined from the simulated tests using three different approaches as outlined in Section 4.3.6.

The points of phase transformation, peak stress ratio, and ultimate stress ratio are marked on the stress paths in Figures 5.11a to 5.11c. The values derived from the simulations are compared with the values derived from the experimental data as presented in Figures 5.11d and 5.11d. The results show good agreement with the experimental results except for OC samples of material type III.

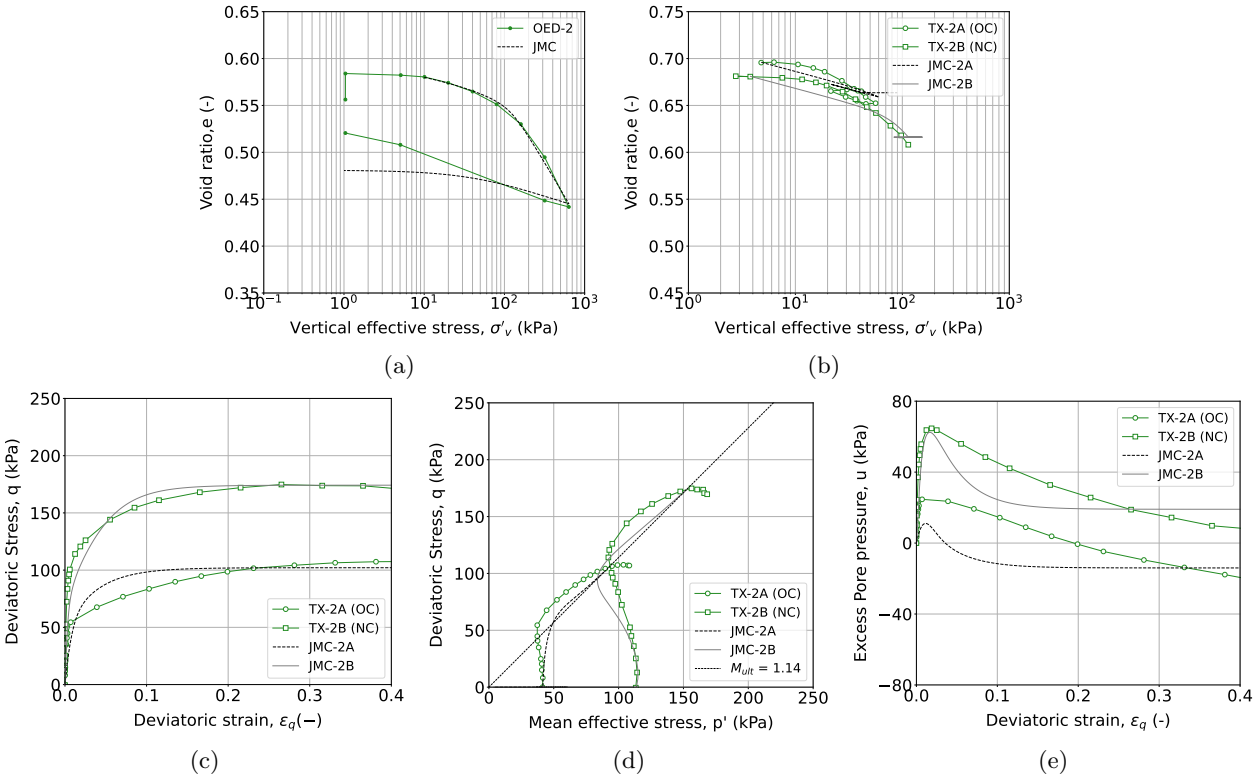

Figure 5.10: Comparison between experimental data and numerical results of material type II

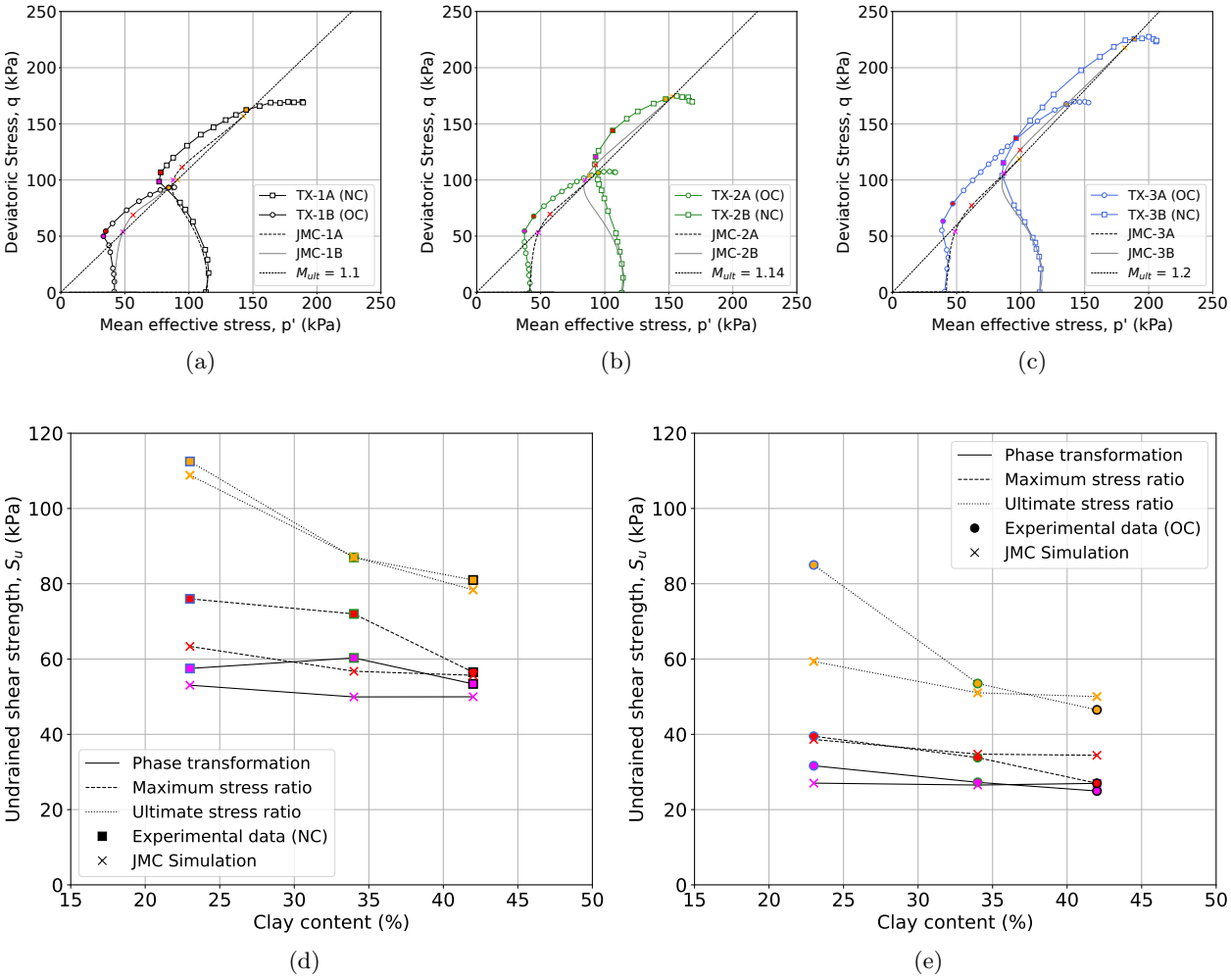

Figure 5.11: Comparison between undrained shear strength estimated from experimental and numerical results - stress path with points marked at phase transformation (magenta), peak stress ratio (red), and ultimate stress ratio (orange)

5.6 Discussion

The results in this chapter demonstrate the JMC-clay BS model's effectiveness in capturing the response of materials with varying compositions under various stress paths. The advanced features of the model accurately predict both pre-failure and failure behaviour. However, utilising the full potential of this modelling framework necessitates the calibration of 15 parameters. While most can be calibrated with a simple laboratory testing scheme, accurate stress state initialisation requires a more extensive set of complex tests. It is important to also note that the swelling observed in the experimental study upon saturation or wetting is believed to alter the initial stress state of the soil which is not accounted for in the current modelling approach.

Chapter 6

Conclusions & Recommendations

This research was motivated by the pressing need to reassess existing construction practices in dike reinforcement. It aims to move beyond the traditional suitability assessment of local soil, and towards an approach that encourages ground-driven design, driven by sustainability considerations. This experimental study characterised the mechanical behaviour of a range of materials used in dike reinforcement, with varying suitability according to existing standards, and explored the potential of soil mixing to improve unsuitable soils. A comparative analysis was conducted to identify the behavioural differences across three materials. This experimental data was then utilised to assess the predictive capabilities of an advanced constitutive model for a range of soil compositions.

The conclusion below outlines the work done in this research while answering the research questions proposed in Section 3.1, following that, recommendations for future work will be suggested.

6.1 Conclusions

Three material types were utilised in this experimental study:

- Type I, with a clay content of 42% and classified as with high resistance to erosion.
- Type III, with a clay content of 23% classified with low resistance to erosion.
- Type II, with a clay content of 34% being an intermediate material that is on the borderline of being classified as erosion-resistant or moderately erosion-resistant. Essentially, Type II represents the minimum erosion resistance requirements for dike reinforcement according to Dutch standards.

The organic content of the three materials ranged between 3.88% and 5.74%. Three laboratory-prepared mixtures with varying ratios were also assessed to determine which mixture closely resembles the properties of the intermediate material. Tests revealed that while Mix II (1:1 ratio of Type I to Type III) had the closest clay content to material Type II, Mix III (4:1) had the closest fine content. While both mixtures are classified as erosion-resistant clay according to Dutch standards, Mix III (4:1) is most closely aligned with the properties of the intermediate material type II, in terms of erodibility.

A closer examination of the soil structure through scanning electron microscopy supports the classification of material Type I as erosion-resistant clay, given its dense structure and smaller pores. In Type I, clay particles were observed to form connectors between sand and silt particles, in contrast to Type III, which exhibited a more open and less dense structure, with clay particles partially coating the silt and sand particles. The observed shrinkage cracks in material Types I and II suggest their susceptibility to degradation upon drying, a feature not observed in Type III.

Following the material characterisation and fabric identification, a mechanical testing campaign was carried out to understand the compression and shear response of the materials through a series of oedometer and triaxial compression tests. The compression response indicates a dependence of compressibility on clay content. The compression index and swell index from 1D compression tests increased from 0.107 to 0.193 and 0.020 to 0.039, respectively, as the clay content increased from 23% to 42%. A difference in compressibility was observed between isotropic and 1D compression tests. In addition to the directional dependencies of soil, this difference could also be attributed to the varying degrees of swelling observed during the saturation stage of triaxial and oedometer tests.

The material response to undrained shear was characterised by strain hardening, with samples exhibiting both clay-like (contraction) and sand-like (dilation) behaviour, with samples of the highest sand content exhibiting the largest dilation. Samples of material types I and II reached similar ultimate stress ratios corresponding to a friction angle of 28^o, while Type III attained a higher ultimate stress ratio corresponding to a friction angle of 30^o.

It is important to note that triaxial samples acted as representative volume elements (RVEs) only up to a certain strain level. Beyond this point, localised deformations became prominent, as shown by post-test CT scans. This suggests that parameters derived at high strain levels should be interpreted with caution, as end restraint effects can introduce bias, affecting their accuracy and representativeness.

An exploration of various methods for deriving undrained shear strength from experimental data revealed that approaches using the points of transformation from contractive to dilative behaviour or peak stress ratio yield consistent and comparable results across the three tested materials. In contrast, methods relying on the ultimate stress ratio at larger strains raise concerns about the triaxial test's representativeness as a volume element. This underscores the need for clear guidelines in deriving undrained shear strength from laboratory tests.

By characterising the mechanical behaviour of the three materials, and identifying the differences observed between them, the main research question is answered. Given the consistent shear response among the three materials, despite their varying levels of erodibility, efforts should focus on enhancing erosion resistance through sustainable solutions. One practical approach is the use of erosion control geomats, which can protect the dike surface until vegetation is fully effective in shielding the cover from erosion.

Based on the composition and erodibility assessment of the soil mixtures, Mix III (4:1 ratio of type I to III) most closely resembles material type II. The observed microstructure of material type II and its close resemblance to that of type I, suggests that that such materials may be suitable for dike construction when linking microstructural features to behavioural characteristics. Lastly, based on the compression and shear response, materials of type I (42% clay) and II (34% clay) demonstrated nearly identical shear behaviour, suggesting comparable performance, while their compressibility was dependent on the clay content. These findings suggest that soil mixing could be a viable solution for utilising local soils that do not meet erosion resistance requirements, thereby answering the first sub-question. However, it is important to note that the laboratory-prepared mixtures are not fully representative of in situ conditions, both in terms of mixing techniques (dry vs. wet) and soil heterogeneity.

Finally, to answer the second and last subquestion, numerical simulations demonstrated the capability of the JMC-clay BS model in capturing both pre-failure and failure responses of materials with varying compositions, across various loading and unloading stress paths which is essential for engineering applications. The effectiveness of the model stems from its features, including bounding surface plasticity, mixed distortional and volumetric hardening, and rotational hardening to account for anisotropy. Through calibrating the model, the isotropic formulation with a modified bounding surface and plastic potential shape, or an anisotropic formulation could capture most of the observed sample response. However, the anisotropic formulation, while accurately representing material behaviour, introduces greater complexity and necessitates additional testing to assess anisotropy evolution for improved stress initialisation and calibration.

6.2 Recommendations

Based on the findings of this study, the following recommendations are proposed for future work:

- **Compaction Techniques:**
  Extend the study to include compaction techniques that more closely resemble those used in the field. As suggested by Jommi and Sciotti (2002), a difference in the microstructure between laboratory and field compacted samples could lead to behavioural differences. Kneading compaction could serve as a good alternative as it can effectively simulate the compaction action of field equipment (Kouassi et al., 2000).

- **Soil Mixing:**
  Further explore soil mixing as a viable solution by replicating field mixing techniques and testing multiple samples mixed and compacted in situ to assess homogeneity.

- **Water Quality:**
  Investigate the use of demineralised water in sample preparation by conducting a hydrometer test to evaluate the impact of tap water or saline water on particle flocculation. Additionally, assess basic index properties like liquid and plastic limits, and build-up to investigate more complex tests if required.

- **Model Calibration and Testing:**
  Conduct active K_0 compression tests to enhance stress-state initialisation in simulations, potentially improving model calibration. Explore additional stress paths to confirm the anisotropic nature of the compacted samples and refine model parameters. In addition, account for the effect of swelling during saturation on the initial stress state of the soil. Once a thorough understanding of saturated material behaviour is established, extend the study to encompass partially saturated conditions using advanced testing equipment and modelling.

Bibliography

Anantanasakul, P., & Roth, C. (2018). Undrained behavior of silt-clay transition soils with varying degrees of overconsolidation. *Journal of GeoEngineering*, *13*(1), 1–12. https://doi.org/10.6310/jog.201803{_}13(1).1

Anantanasakul, P., Yamamuro, J. A., Asce, M., & Kaliakin, V. N. (2012). Stress-Strain and Strength Characteristics of Silt-Clay Transition Soils. https://doi.org/10.1061/(ASCE)

ASTM D2974-14. (2014). *Standard Test Methods for Moisture, Ash, and Organic Matter of Peat and Other Organic Soils*. American Society for Testing; Materials.

Barden, L., & McDermott, R. J. W. (1965). Use of Free Ends in Triaxial Testing of Clays. *Journal of the Soil Mechanics and Foundations Division*, *91*(6), 1–23. https://doi.org/10.1061/JSFEAQ.0000806

Barden, L., & Sides, G. R. (1970). Engineering Behavior and Structure of Compacted Clay. *Journal of the Soil Mechanics and Foundations Division*, *96*(4), 1171–1200. https://doi.org/10.1061/JSFEAQ.0001434

Barnes, G. E. (2018). Workability of clay mixtures. *Applied Clay Science*, *153*, 107–112. https://doi.org/10.1016/j.clay.2017.12.006

Basma, A. A., Al-Homoud, A. S., & Al-Tabari, E. Y. (1994). Effects of methods of drying on the engineering behavior of clays. *Applied Clay Science*, *9*(3), 151–164. https://doi.org/https://doi.org/10.1016/0169-1317(94)90017-5

Briaud, J.-L., Shafii, I., Chen, H.-C., & Medina-Cetina, Z. (2019). *Relationship Between Erodibility and Properties of Soils* (tech. rep.). National Academius of Sciences, Engineering, and Medicine. Washington, DC. https://doi.org/https://doi.org/10.17226/25470

BS1377. (1996). *Methods of Test for Soils for Civil Engineering Purposes Part 2. Classification Tests*. British Standard Institution.

Chao, C. (2024). *Laboratory Investigation and Constitutive Modelling of Dutch Organic Clays (Manuscript under review)* [Doctoral dissertation, Delft University of Technology].

Cola, S., & Simonini, P. (2002). Mechanical behavior of silty soils of the Venice lagoon as a function of their grading characteristics. *Canadian Geotechnical Journal*, *39*(4), 879–893. https://doi.org/10.1139/t02-037

Collins, K., & McGown, A. (1974). The form and function of microfabric features in a variety of natural soils. *Géotechnique*, *24*(2), 223–254.

Dafalias, Y. F., & Taiebat, M. (2013). Anatomy of rotational hardening in clay plasticity. *Geotechnique*, *63*(16), 1406–1418. https://doi.org/10.1680/geot.12.P.197

Dafalias, Y. F. (1981). The Concept and Application of the Bounding Surface in Plasticity Theory. https://api.semanticscholar.org/CorpusID:118638008

Dafalias, Y. F., Manzari, M. T., & Papadimitriou, A. G. (2006). SANICLAY: Simple anisotropic clay plasticity model. *International Journal for Numerical and Analytical Methods in Geomechanics*, *30*(12), 1231–1257. https://doi.org/10.1002/nag.524

Das, B. M. (2019). *Advanced Soil Mechanics, Fifth Edition* (5th). CRC Press. https://doi.org/10.1201/9781351215183

Delft. (1996). *CLAY FOR DIKES* (tech. rep.). www.minvenw.nl/dww/home/

Delgromij. (n.d.). https://www.delgromij.nl/

den Heijer, F., & Kok, M. (2024). Risk based portfolio planning of dike reinforcements. *Reliability Engineering and System Safety*, *242*. https://doi.org/10.1016/j.ress.2023.109737

Dibernardo, A., & Purdue, C. W. L. (1979). *The Effect of Laboratory Compaction on the Compressibility of Compacted Highly Plastic Clay : Interim Report. Publication FHWA/IN/JHRP-79/03* (tech. rep.). Joint Highway Research Project, Indiana Department of Transportation and Purdue University. West Lafayette, Indiana.

Duncan, J. M., & Dunlop, P. (1968). The Significance of Cap and Base Restraint. *Journal of the Soil Mechanics and Foundations Division*, *94*, 271–290. https://api.semanticscholar.org/CorpusID:138048109

Fell, R., Hanson, G., Herrier, G., Marot, D., & Wahl, T. (2013). Relationship between the erosion properties of soils and other parameters. *Erosion in Geomechanics Applied to Dams and Levees*. https://doi.org/10.1002/9781118577165.ch5

Fugro. (2021). *POV Dijkversterking met gebiedseigen grond Fase 2 'best practices' Nederland V3* (tech. rep.). Roermond, Netherlands.

Fukushima, S., & Tatsuoka, F. (1984). Strength and Deformation Characteristics of Saturated Sand at Extremely Low Pressures. *Soils and Foundations*, *24*(4), 30–48. https://doi.org/https://doi.org/10.3208/sandf1972.24.4{_}30

Gibbs, H. J. (1962). *A Study of Erosion and Tractive Force Characteristics in Relation to Soil Mechanics Properties: Earth Research Program* (tech. rep. No. EM-643). U.S. Department of the Interior, Bureau of Reclamation, Division of Engineering Laboratories. Denver, Colo.

Guerra, A. (1994). The effect of organic matter content on soil erosion in simulated rainfall experiments in W. Sussex, UK. *Soil Use and Management*, *10*(2), 60–64. https://doi.org/10.1111/j.1475-2743.1994.tb00460.x

Handboek Dijkenbouw (tech. rep.). (2018). www.isso.nl

Hanson, G. J. (1992). Erosion Resistance of Compacted Soils. *Transportation Research Record*, (1369).

Hodek, R. J. (1972). *Mechanism for Compaction and Response of Kaolinite: Final Report* (tech. rep. No. FHWA/IN/JHRP-72/36). Joint Highway Research Project, Indiana Department of Transportation and Purdue University. West Lafayette, Indiana. https://docs.lib.purdue.edu/jtrp/1400/

HWBP. (2023). Het Hoogwaterbeschermingsprogramma (HWBP). https://www.hwbp.nl/

Johnson, J. M., & Purdue, C. W. L. (1979). *The Effect of Laboratory Compaction on the Shear behaviour of a Highly Plastic Clay After Saturation and Consolidation : Interim Report. Publication FHWA/IN/JHRP-79/07* (tech. rep.). Joint Highway Research Project, Indiana Department of Transportation and Purdue University. West Lafayette, Indiana. https://doi.org/10.5703/1288284313990

Jommi, C., & Sciotti, A. (2002). A study of the microstructure to assess the reliability of laboratory compacted soils as reference material for earth constructions. In F. Bontempi (Ed.), *Proceedings of isec-02* (pp. 2409–2415, Vol. 3). A.A. Balkema Publishers.

Kouassi, P., Breysse, D., Girard, H., & Poulain, D. (2000). A New Technique of Kneading Compaction in the Laboratory. *Geotechnical Testing Journal*, *23*(1), 72–82. https://doi.org/10.1520/GTJ11125J

Kruse, G. (1986). *Onderzoek van kleibekleding van dijken langs IJssel en Pannerdens Kanaal voor het ontwikkelen van keuringseisen van klei* (tech. rep. No. CO-275921/47). Grondmechanica Delft.

Kruse, G. (1987). *Onderzoek van kleibekleding van dijken aan zout en brak water in Friesland, Zuid-Holland en Zeeland voor het ontwikkelen voor keuringseisen van klei* (tech. rep. No. CO-275923/29). Grondmechanica Delft.

Kruse, G. (1988). *Onderzoek naar het beoordelen van de geschiktheid van kleigrond voor bekleding van dijken met grasdekking* (tech. rep. No. CO-275925/14). Grondmechanica Delft.

Ladd, C. C. (1960). Mechanisms of Swelling by Compacted Clay. *Highway Research Board bulletin*. https://api.semanticscholar.org/CorpusID:92970448

Lade, P. V. (2016). *Triaxial Testing of Soils*. John Wiley; Sons.

Lambe, T. W. (1958). The Structure of Compacted Clays. *Journal of the Soil Mechanics and Foundations Division*, *84*(2), 1654–1. https://doi.org/10.1061/JSFEAQ.0000114

Lyle, W. M., & Smerdon, E. T. (1965). Relation of Compaction and Other Soil Properties to Erosion Resistance of Soils. *Transactions of the ASABE*, *8*, 419–422.

Mcdowell, G. R., & Hau, K. W. (2003). *A simple non-associated three surface kinematic hardening model* (tech. rep. No. 4).

Mitchell, J. K. (1976). *Fundamentals of Soil Behavior*. Wiley. https://books.google.nl/books?id=R_ZRAAAAMAAJ

Monkul, M. M., & Ozden, G. (2007). Compressional behavior of clayey sand and transition fines content. *Engineering Geology*, *89*(3-4), 195–205. https://doi.org/10.1016/j.enggeo.2006.10.001

Mostafa, T. S., Imran, J., Chaudhry, M. H., & Kahn, I. B. (2008). Erosion Resistance of Cohesive Soils. *Journal of Hydraulic Research*, *46*(6), 777–787. https://doi.org/10.1080/00221686.2008.9521922

Muir Wood, D., & Kumar, G. V. (1999). Experimental observations of behaviour of heterogeneous soils. *Mechanics of Cohesive-frictional Materials*, *5*, 373–398.

Muraro, S., & Jommi, C. (2021). Pre-failure behaviour of reconstituted peats in triaxial compression. *Acta Geotechnica*, *16*(3), 789–805. https://doi.org/10.1007/s11440-020-01019-2

Muraro, S. (2019). *The deviatoric behaviour of peat: a route between past empiricism and future perspectives* [Doctoral dissertation, Delft University of Technology]. https://doi.org/10.4233/uuid:ffbea4e0-2e97-4d41-819d-beec42120b29

Netherlands Environment Assessment Agency. (2019). Correctie Formulering Over Overstromingsrisico Nederland in IPCC-Rapport. https://www.pbl.nl/correctie-formulering-over-overstromingsrisico-nederland-in-ipcc-rapport

Nocilla, A., Coop, M. R., & Colleselli, F. (2006). The mechanics of an Italian silt: An example of 'transitional' behaviour. *Geotechnique*, *56*(4), 261–271. https://doi.org/10.1680/geot.2006.56.4.261

Nova, R. (1977). On the hardening of soils. *Archiwum Mechaniki Stosowanej*, *29*, 445–458.

Nova, R., & Wood, D. M. (1979). A constitutive model for sand in triaxial compression. *International Journal for Numerical and Analytical Methods in Geomechanics*, *3*, 255–278.

Paaswell, R. E. (1973). Causes and Mechanisms of Cohesive Soil Erosion: The State of the Art. *Highway Research Board Special Report*. https://api.semanticscholar.org/CorpusID:130320217

Prakash, K., Sridharan, A., & Prasanna, H. S. (2014). Compaction Induced Yield Stress. *Geotechnical and Geological Engineering*, *32*(2), 311–319. https://doi.org/10.1007/s10706-013-9715-6

Rochelle, P. L., Leroueil, S., Trak, B., Blais-Leroux, L., & Tavenas, F. (1988). Observational Approach to Membrane and Area Corrections in Triaxial Tests. *ASTM special technical publications*, 715–731. https://api.semanticscholar.org/CorpusID:107667692

Rowe, P. W., & Barden, L. (1964). Importance of Free Ends in Triaxial Testing. *Journal of Soil Mechanics & Foundations Div*, *90*, 1–28. https://api.semanticscholar.org/CorpusID:135017435

Schaafsma-Tilstra, M. (2014). *Man-made Lowlands; A Future for ancient dykes in the Netherlands* (tech. rep.). Rijksdienst voor het Cultureel Erfgoed. Amersfoort.

Seidalinov, G. (2018). *Constitutive and Numerical Modeling of Clay Subjected to Cyclic Loading* [Doctoral dissertation].

Shi, Z., Finno, R. J., & Buscarnera, G. (2018). A hybrid plastic flow rule for cyclically loaded clay. *Computers and Geotechnics*, *101*, 65–79. https://doi.org/10.1016/j.compgeo.2018.04.018

Skempton, A. W. (1944). Notes on the compressibility of clays. https://doi.org/10.1144/GSL.JGS.1944.100.01-04.08

Sridharan, A., Abraham, B. M., & Jose, B. T. (1991). Improved technique for estimation of preconsolidation pressure. *Geotechnique*, *41*, 263–268. https://doi.org/10.1680/geot.1991.41.2.263

Terzaghi, K., & Peck, R. (1967). *Soil Mechanics in Engineering Practice*. Wiley.

VandenBerge, D. R., Brandon, T. L., & Duncan, J. M. (2014). Triaxial tests on compacted clays for consolidated-undrained conditions. *Geotechnical Testing Journal*, *37*(4). https://doi.org/10.1520/GTJ20130202

Verhaegen, T. H. (1984). The Influence of Soil Properties on the Erodibility of Belgian Loamy Soils: A Study Based on Rainfall Simulation Experiments. *Earth Surface Processes and Landforms*, *9*(6), 499–507.

Wiggers, A., & Peters, D. (2021). *Grondgestuurd ontwerpen; "Best Practices" Internationaal* (tech. rep.). Royal HaskoningDHV.

Wood, D. M. (2014a, October). Index properties. In *Soil behaviour and critical state soil mechanics* (pp. 256–309). Cambridge University Press. https://doi.org/10.1017/cbo9781139878272.010

Wood, D. M. (2014b, October). Plasticity and yielding. In *Soil behaviour and critical state soil mechanics* (pp. 55–83). Cambridge University Press. https://doi.org/10.1017/cbo9781139878272.004

Yang, S., Sandven, R., & Grande, L. (2001). Undrained behaviour of silt. *International Society of Soil Mechanics and Geotechnical Engineering*. https://www.issmge.org/publications/online-library

Yin, J.-H. (1999). Properties and behaviour of Hong Kong marine deposits with different clay contents. *Canadian Geotechnical Journal*, *36*(6), 1085–1095. https://doi.org/10.1139/t99-068

Appendix A

Sensitivity Analysis

A sensitivity analysis was performed on the calibrated JMC-clay BS parameters for material type I. A triaxial compression tests is selected for the sensitivity analysis. The simulation process involved isotropic compression stage, where (p') is incrementally increased to 113 kPa, followed strain controlled undrained shearing to 40%. This replicates the test performed on sample TX-1A in Chapter 4.

The following initial state parameters were used in the analysis:

- Initial mean effective stress, p' of 6.5 kPa.
- Initial size of the bounding surface, p'_0 of 81 kPa.
- Initial inclination of the bounding surface, α_i of 0.404.
- Initial void ratio, e of 0.723

The influence of parameters D_0, D_1, p'_0, and c are presented below. As mentioned in Chapter 5, given the fact that the experimental study did not include cyclic triaxial tests, no elastic nucleus was adopted (s_{eln}=1), and parameters defining define the cyclic degradation/shakedown (a_d, w) were set to 0. The model parameters adopted in the sensitivity analysis are reported in Table A.1, and the results are presented in Figures A.1 to A.4.

Table A.1: Model parameters adopted in sensitivity analysis

Sensitivity parameter	λ	κ	$M_{g,c}$	$M_{g,e}$	ν	c	z_c	z_e	s	y	$M_{f,c}$	k_f	D_0	D_1	h_0
D_0	0.084	0.017	1.10	0.9	0.3	90	1.6	1.2	2.2	2	1.10	2.00	-	25	150
D_1	0.084	0.017	1.10	0.9	0.3	90	1.6	1.2	2.2	2	1.10	2.00	0.45	-	150
p'_0	0.084	0.017	1.10	0.9	0.3	90	1.6	1.2	2.2	2	1.10	2.00	0.45	25	150
c	0.084	0.017	1.10	0.9	0.3	-	1.6	1.2	2.2	2	1.10	2.00	0.45	25	150

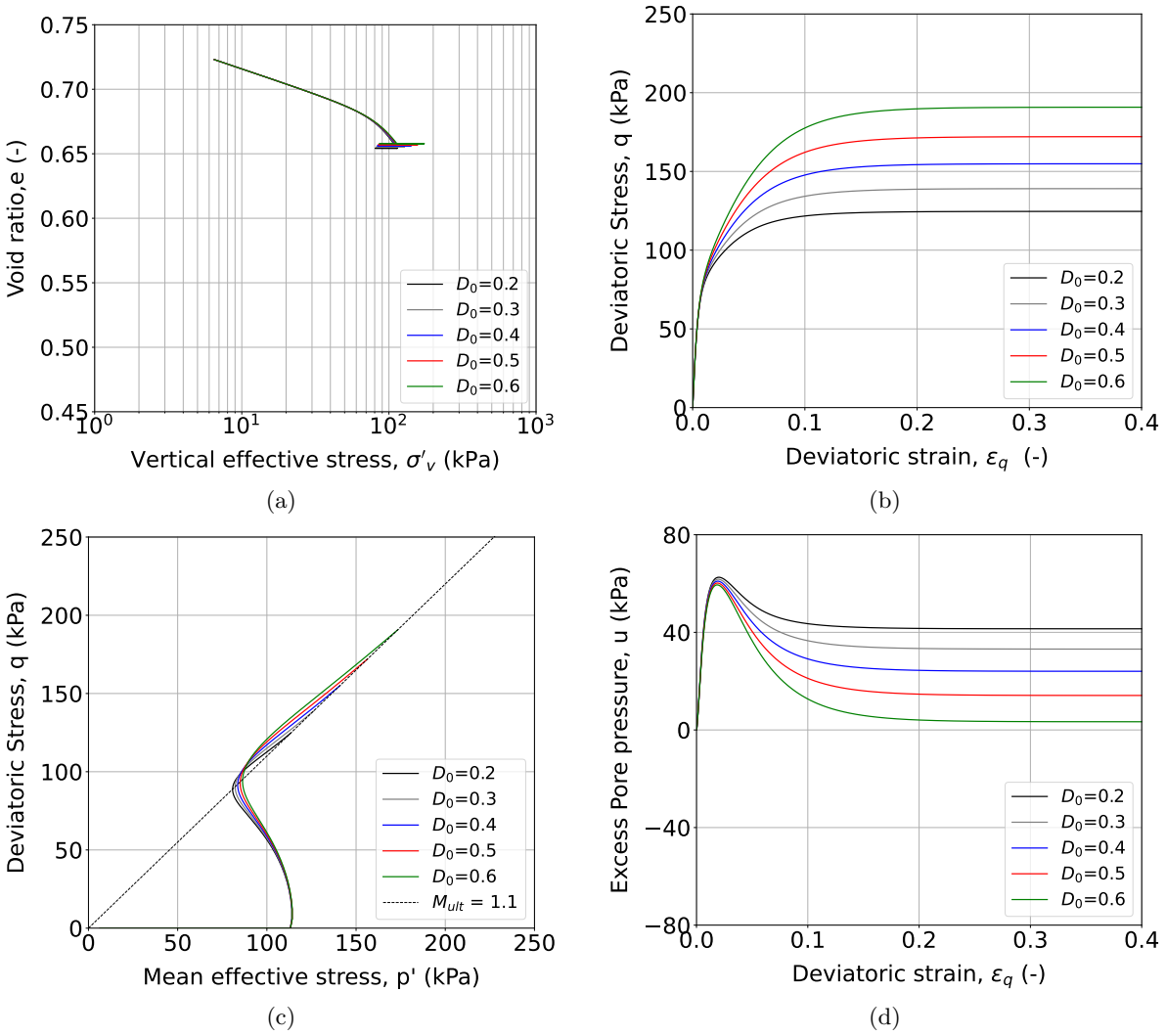

Figure A.1: Sensitivity analysis results demonstrating the influence of parameter D_0 on (a) Void ratio evolution, (b) Stress-strain behavior, (c) Stress path, and (d) Excess pore pressure generation during isotropic compression and strain-controlled undrained shear

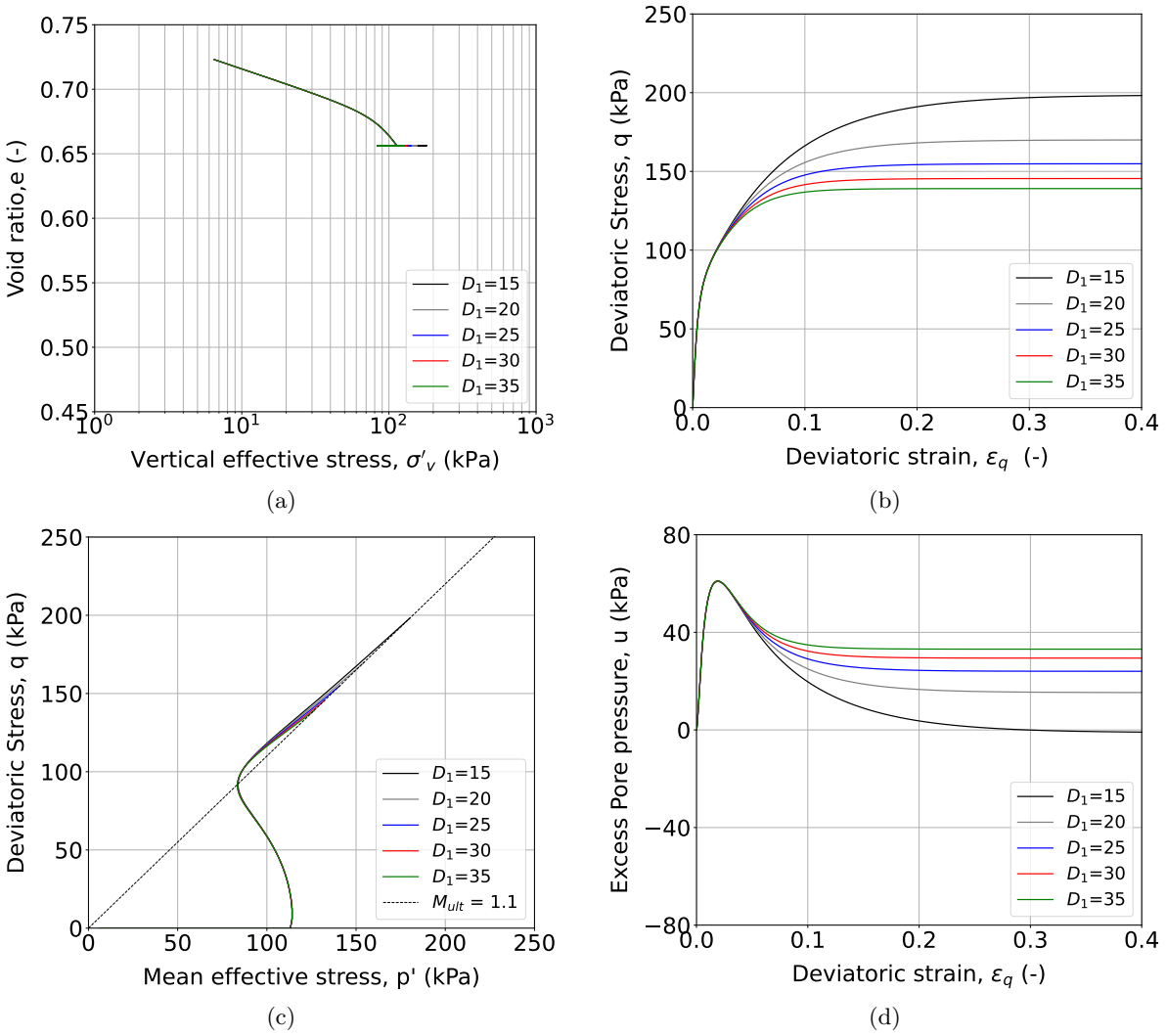

Figure A.2: Sensitivity analysis results demonstrating the influence of parameter D_1 on (a) Void ratio evolution, (b) Stress-strain behavior, (c) Stress path, and (d) Excess pore pressure generation during isotropic compression and strain-controlled undrained shear

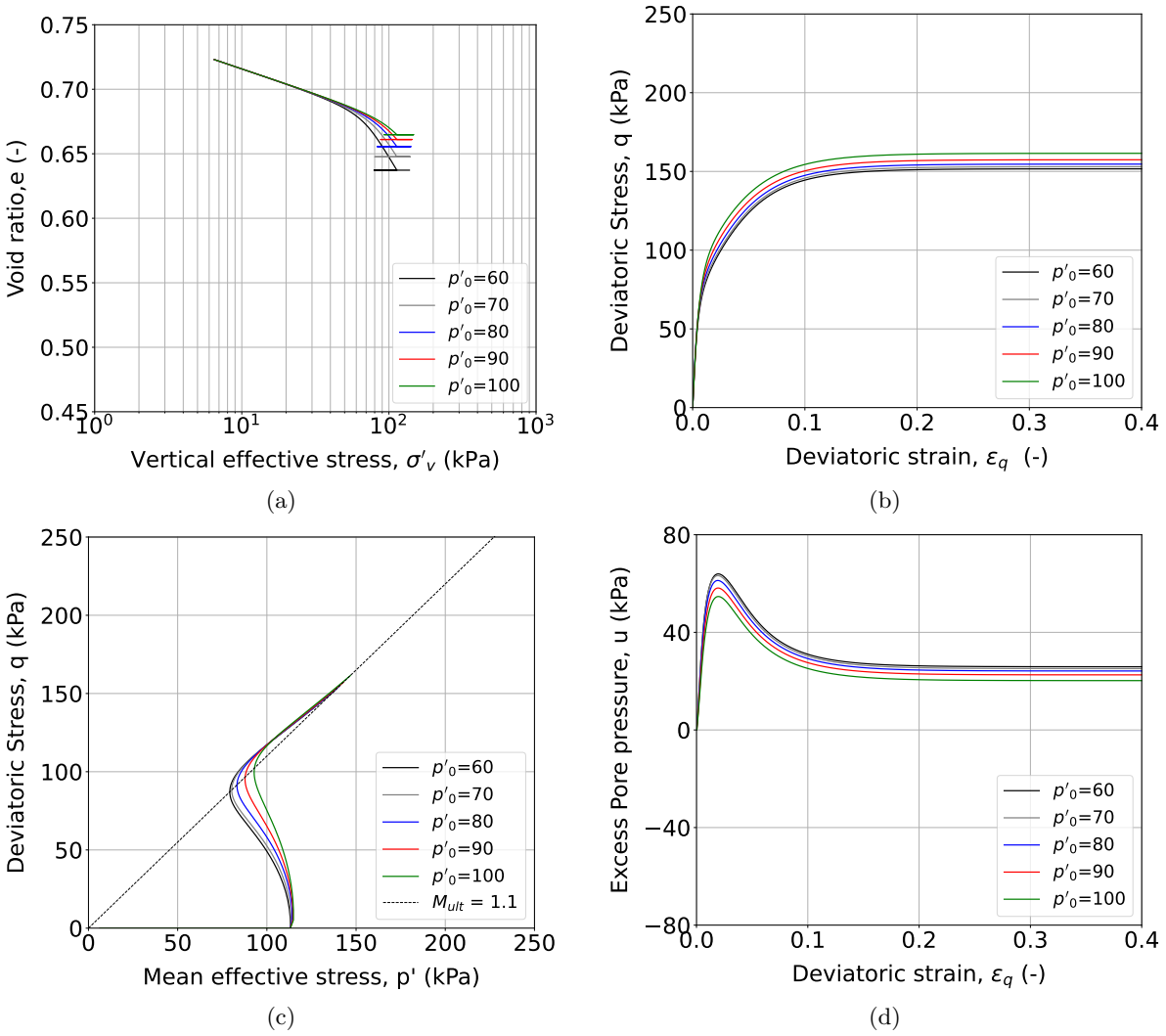

Figure A.3: Sensitivity analysis results demonstrating the influence of parameter p'_0 on (a) Void ratio evolution, (b) Stress-strain behavior, (c) Stress path, and (d) Excess pore pressure generation during isotropic compression and strain-controlled undrained shear

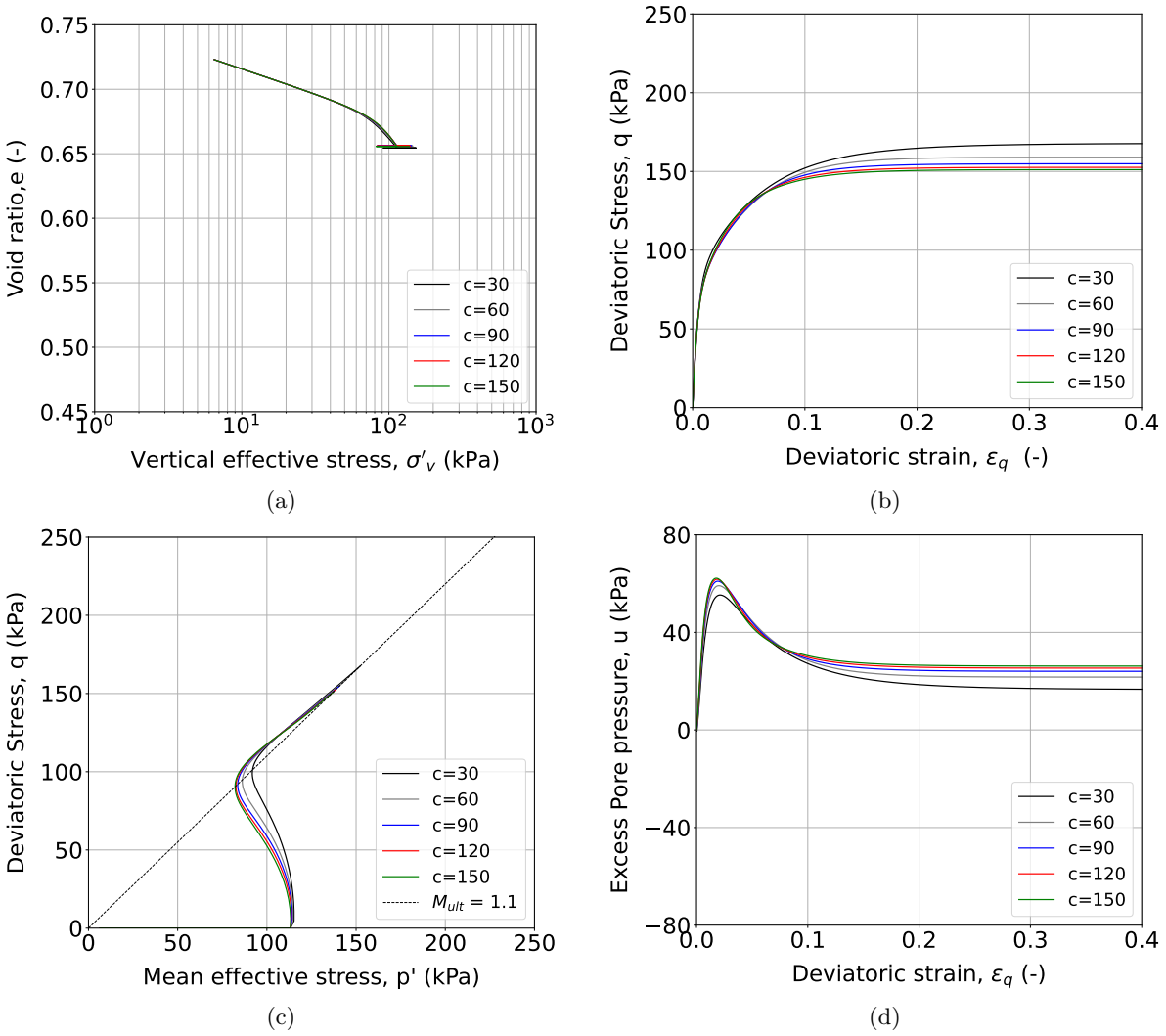

Figure A.4: Sensitivity analysis results demonstrating the influence of parameter c on (a) Void ratio evolution, (b) Stress-strain behavior, (c) Stress path, and (d) Excess pore pressure generation during isotropic compression and strain-controlled undrained shear